Dosimetric and Biological Validation of a Proton Therapy Research Line using a Murine-Based Phantom

MSc Thesis

Michèle Knol

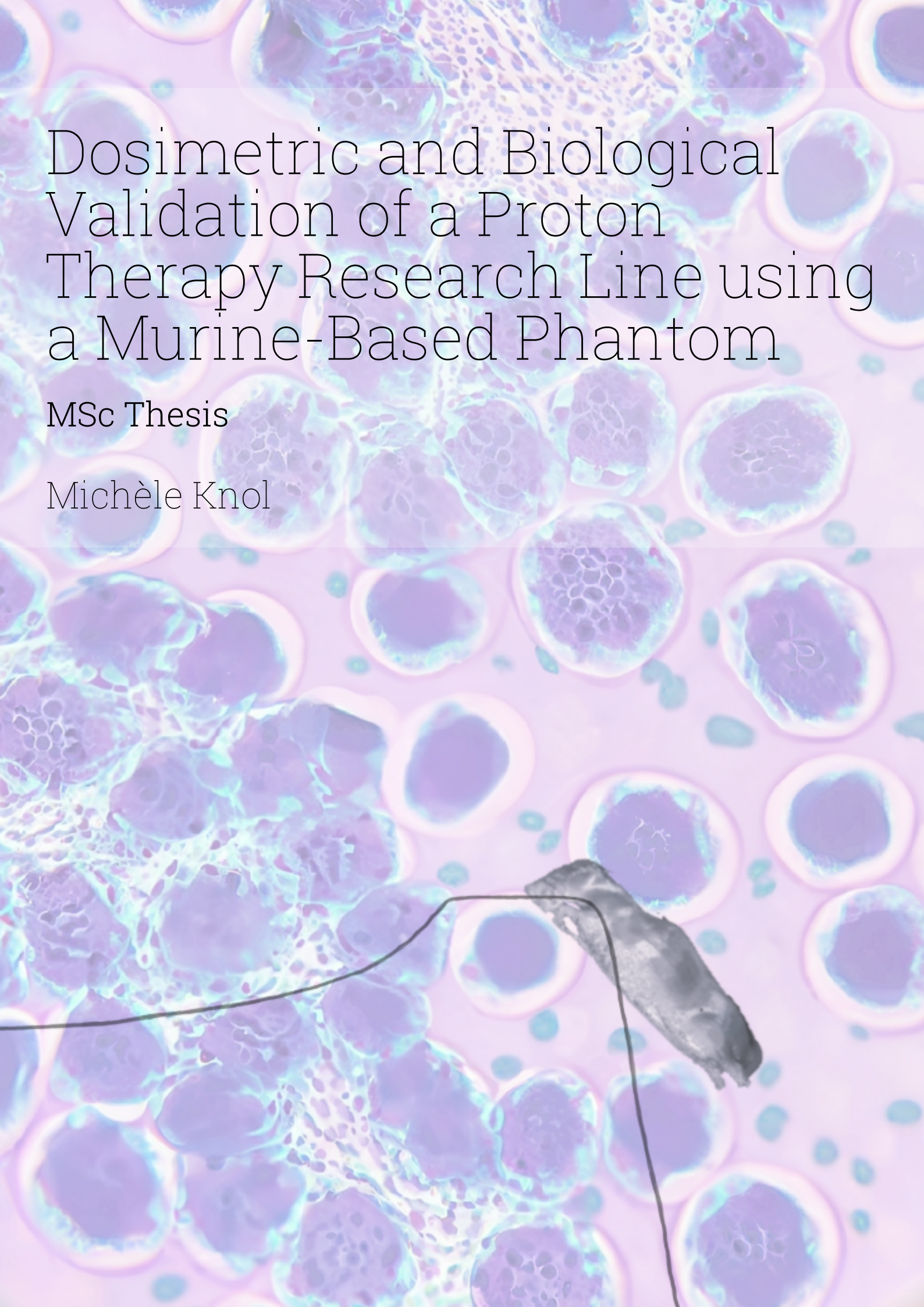

Dosimetric and Biological Validation of a Proton Therapy Research Line using a Murine-Based Phantom

MSc Thesis

by

Michèle Knol

to obtain the degrees of

Master of Science in Biomedical Engineering
and
Master of Science in Nanobiology

at the Delft University of Technology,
to be defended on August 30, 2023, at 12:00.

Student number: 4962567
Project duration: November, 2022 – August, 2023

Thesis committee:

Prof. Dr. Mischa Hoogeman	HollandPTC & TUDelft	Supervisor
Dr. Jeroen Essers	Erasmus MC & TUDelft	Supervisor
Ir. Tim Heemskerk	Erasmus MC	Daily supervisor
Dr. Steven Habraken	Erasmus MC & HollandPTC	Daily supervisor
Dr. Alex Zelenskyy	ErasmusMC	External committee member
Dr. Ir. Danny Lathouwers	TUDelft	External committee member

Erasmus MC Cancer Institute

TU Delft

HollandPTC Proton Therapy Centre

Preface

Let's start with the story of how I came here. I've always had an interest in the human body and medicine in particular, but also in research, especially when done myself. In 2015, when my grandpa got a braintumour, but still participated in a clinical study, I knew that I wanted to do research somewhere in that field, to try to understand everything a bit better. Somewehere around 2016 I saw HollandPTC on TV and knew that I was going to try to do an internship in the radiotherapy field, preferably there. So I switched from the somewhat general bachelor Biology to the more technical master Biomedical Engineering, the medical physics track. However, then I missed being in the lab, so I went on and did the master Nanbiology alongside it. Fast-forward to now: I am finishing up both masters at the place where my inspiration started!

For the last, almost exactly, year, I've worked on this project with a lot of enthousiasm. I loved coming here to work on this and I loved how much I was able to think without limits. Finally, after all these years of school and university, I could work on something big myself without set boundaries. I have learned so much this past year, a lot of it within the radiotherapy and radiobiology, but almost equally as much about myself, what I want and what will make me happy. After this past year, I am absolutely sure that I want to pursue a career in the academic world and just play and learn and experiment.

But of course, I did not do this project on my own and I did not learn everything by myself. So on to the acknowledgement part, which are quite a lot of people. First, of course, my supervisors, who gave me this project. Tim, thank you for learning me the labtechniques and other stuff, for always discussing weird results with me for way too long, and for answering all my messages really really fast! Steven, thank you for the very interesting weekly discussions, in which you would always answer every question that I had regarding this subject. Thank you Jeroen en Mischa for making me look more critical to my own work. Then on to HollandPTC. Thank you Marta for all the discussions that we've had. I've learned a lot from you and I really enjoyed the experiments we did together! Thank you to Ernst for the many, many prints you came up with and printed. Eva, thank you for all the discussion we had in the beginning, you've left a really interesting project for me! I also wanted to thank Robin Nadar, who learned us how to make the spheroids, the people from AMIE with whom I got to make some CT scans of the phantom, and all the people from the radiotherapy department and both proton meetings for all your interesting insights.

Also thanks to the other masterstudents of the radiotherapy department, especially Manon, Suzanne, Linda, and Odin. I really liked coming here, even when the stress levels in this room were quite high. I loved how we could just talk on and on and on about everything and also nothing at all. It really helped how even when some things did not go the way it was planned, we could all support each other and make it positive within a few minutes. Also thank you for accepting that I could not stop talking some days, haha. And lastly, thanks to my family and friends. Thank you for trying to distract me with fun stuff, even though my head went 24/7 back to my project. En dan echt als allerlaatste: mama, dankjewel dat je altijd in mij geloofde, ook al was je af en toe een van de weinigen. Dankje dat je altijd hebt geluisterd naar wat ik wilde en wilde en er dan alles aan deed om dat te laten gebeuren. Het is ons gelukt!

Okay, now that we've had all the acknowledgements, have fun reading this thesis!

Michèle Knol
Delft, August 2023

Abstract

During pre-clinical research on proton therapy, validating the dosimetry is important for accurate and representable results. To ensure that research outcomes can eventually be implemented in clinical practices, it is equally as important to also take biological effects into account. The aim of this thesis was, therefore, to dosimetrically and biologically commission a pre-clinical proton therapy research line.

A phantom was designed, 3D-printed and irradiated to check accurate positioning in the beamline. Radiochromic film was used as a dosimeter at different positions within the phantom. The blackening of this radiochromic film after proton irradiations was quantified to obtain information on the dosimetry. It seemed that the phantom was correctly positioned at different places in the spread-out Bragg peak. However, accurate and precise dosimetry appeared to be difficult with radiochromic film. The added compensator successfully gave more uniform profiles throughout the whole depth of the phantom.

Furthermore, the dose response of spheroids made from FaDu tumour cells was characterised and compared to the dose response of cells grown as a monolayer. Spheroid growth and viability, based on the cellular ATP levels, were used as biological endpoints. A different dose response of FaDu spheroids was found when compared to that of cells, however, no clear explanation was found and more research remains to be done.

Overall, with some further research, this 3D-printed phantom, along with the tumour spheroids, can be implemented to validate a pre-clinical proton therapy research line.

Contents

List of Figures

List of Tables

Nomenclature

Abbreviations

Abbreviation	Definition
2D	Two-dimensional
3D	Three-dimensional
ASA	Acrylonitrile Styrene Acrylate
ATP	Adenosine Triphosphate
Calcein AM	Calcein Acetoxymethyl ester
CT	Computed Tomography
DMEM	Dulbecco's Modified Eagle's Medium
DNA	Deoxyribonucleic Acid
ECM	Extracellular Matrix
Erasmus MC	Erasmus Medical Center
FCS	Fetal Calf Serum
HollandPTC	Holland Proton Therapy Center
LET	Linear Energy Transfer
OAR	Organ-at-Risk
PBS	Phosphate Buffered Saline
PI	Propidium Iodide
RBE	Relative Biological Effectiveness
RID	Reactor Institute Delft
ROS	Reactive Oxygen Species
RSP	Relative Stopping Power
SOBP	Spread-Out Bragg Peak
WER	Water Equivalent Ratio
WET	Water Equivalent Thickness

1 Introduction

While cancer is still one of the main causes of death [1], our ability to treat this disease has improved significantly over the last couple of decades, due to better techniques, earlier diagnostics and combination therapies [2]. A much-used technique is radiotherapy, where a beam of ionising radiation is used to damage and kill the tumour cells while mostly sparing the healthy tissue surrounding it. The idea behind this is that healthy cells can better repair damage compared to tumour cells [3]. Furthermore, precise irradiations can be performed by utilizing imaging techniques and treatment planning systems. Different ionising particles can be used for radiotherapy, of which photons are most commonly used. However, patients with, for example, head-and-neck cancer that undergo radiotherapy, suffer side effects such as dysphagia (difficulty with swallowing), xerostomia (extremely dry mouth), or trismus (not being able to open the jaw completely) [4]. For such patients, proton therapy can be an outcome, as using protons leads to lower toxicity.

1.1. Physics of Proton Therapy

Protons have a superior dose distribution to conventional photon therapy when it comes to clinical uses. The characteristic mono-energetic depth-dose curve of protons is known as the (pristine) Bragg curve, with the sharp peak at the end of the proton's range called the Bragg peak. When protons enter the material, they gradually lose small amounts of energy through various elastic- and inelastic Coulombic interactions within the material [5]. More energy is deposited by protons with a lower energy. Subsequently, as protons approach the end of their range, the energy of the protons is decreased. Accordingly, their energy loss increases significantly, and all remaining energy is deposited. This implies that low doses are deposited at the entrance of the Bragg curve, followed by a large dose deposition at the peak, with ultimately a sharp distal fall-off. This means that when compared to photons, which deposit energy all throughout their range, protons are able to spare much more surrounding tissue. The depth-dose curves of photons and protons are shown in figure 1.1a.

Nevertheless, the narrow shape of a pristine Bragg peak will not cover a whole tumour. To achieve a homogeneously irradiated tumour volume, a technique called range modulation is employed. The energies of multiple pristine Bragg peaks can be modulated and superimposed to create a spread-out Bragg peak (SOBP), for instance, through implementing a ridge filter [6]. This is built on the notion that by reducing the energy of a proton beam, its range gets shortened. The spread-out Bragg peak is shown in figure 1.1b. The SOBP enables uniform irradiation of the entire tumour volume while mostly sparing the healthy tissues surrounding it. This is particularly advantageous when organs at risk (OARs) are located near the tumour site.

1.1.1. Range Estimation, Stopping Power, and Water Equivalent Thickness

The energy loss of a proton beam can be expressed through the stopping power, which is the rate at which a charged particle loses its energy along the travelled path through a material:

$$S = -\frac{dE}{dx}, \tag{1.1}$$

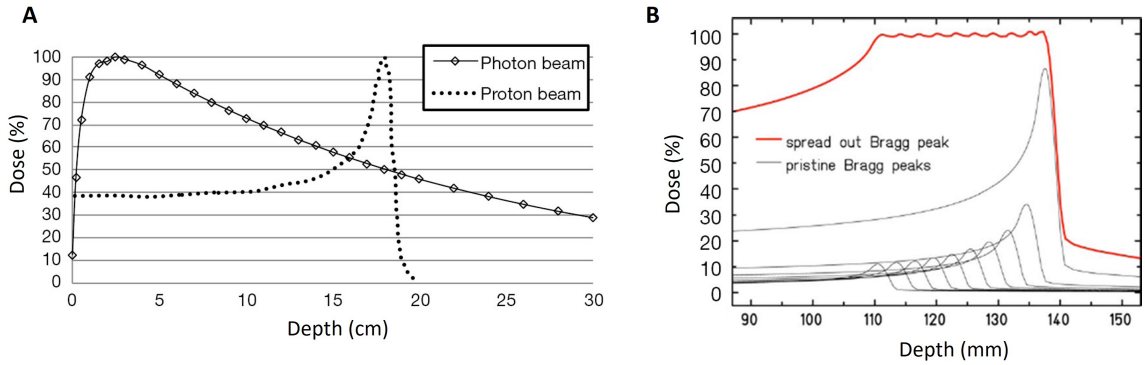

Figure 1.1: The depth-dose curves for photons and protons. **(A)**The depth dose curve of a photon beam compared to that of a mono-energetic proton beam. The proton beam has a much lower entrance dose and almost no dose after its peak, when compared to the photon beam, leading to less dose deposition in the healthy tissues surrounding the tumour. Figure adapted from [7]. **(B)** Superimposing multiple mono-energetic Bragg curves creates a spread-out Bragg peak (SOBP). The SOBP can deliver a uniform dose to the whole tumour while sparing OARs surrounding it. Figure adapted from [8]

where S is the stopping power, E is the energy of the beam, and x is the path length [9]. The energy loss of protons is mainly caused by elastic- and inelastic Coulomb interactions, where part of the energy is transferred to the atomic electrons in the material. Even though nuclear reactions also occur when protons interact with matter, their contribution to the energy loss is negligible [5, 9]. The energy loss of protons can be described with the Bethe-Bloch formula [10]:

$$RSP = \frac{\rho N_g}{\rho_{water} N_{g,water}} \frac{ln\left[2m_e c^2 \beta^2 / I_m \left(1-\beta^2\right)\right] - \beta^2}{ln\left[2m_e c^2 \beta^2 / I_{water}\left(1-\beta^2\right)\right] - \beta^2}, \tag{1.2}$$

with RSP the stopping power of protons in a material relative to the proton stopping power in water, ρ the density, m_e the mass of an electron, c the speed of light in vacuum, and β the velocity of the incident proton relative to the speed of light. N_g represents the number of electrons per unit volume of material and can be calculated by:

$$N_g = N_A \sum \frac{w_i Z_i}{A_i}. \tag{1.3}$$

Here, N_A is Avogadro's number, w_i the atomic weight, Z_i the atomic number, A_i the atomic weight number, and I_m is the mean excitation energy of the atoms, obtained as follows:

$$lnI_m = \frac{\sum \frac{w_i Z_i}{A_i} lnI_i}{\sum \frac{w_i Z_i}{A_i}}, \tag{1.4}$$

with

$$I_i = \begin{cases} I \approx 19.0eV & Z = 1, \\ I \approx (11.2 + 11.7 * Z)\, eV & 2 \leq Z \leq 13, \\ I \approx (52.8 + 8.71 * Z)\, eV & Z > 13. \end{cases} \tag{1.5}$$

It is gained from the Bethe-Bloch equation (eq. 1.2) that the proton stopping power directly depends on the mass density of the material the beam travels through, as well as the atomic composition of the material. This comes into play when range estimations are calculated. Accurate positioning of the Bragg peak is essential, as it is desired that the SOBP fully encompasses the tumour site, but does not cover any healthy tissue. Hence, the determination of the range of the proton beam through all tissues is a crucial step in this process. The range of the protons relies on the stopping power values of all materials encountered along its path. Unlike photons, which have a straightforward stopping power prediction based on CT scans, predicting proton stopping power is considerably more challenging. A relation between the electron density data obtained from CT scans and the material properties needs to be established in order for the proton RSPs to be calculated [9, 11]. Such a relation is established

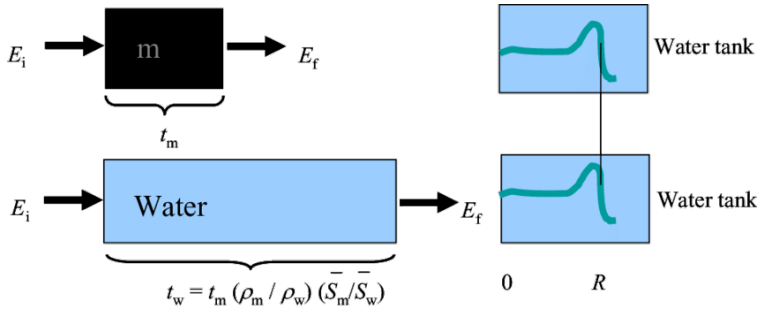

Figure 1.2: The concept of the water equivalent thickness. The water slab achieves a similar range shift as the material. Using water equivalency enables straightforward calculations, as range shifts depend on material properties and will, therefore, be different per material. Figure from [5]

earlier of which the report can be found in Appendix C.

The energy loss and the residual range of protons are commonly expressed in water equivalent thickness (WET) [5]. The WET of a material is defined as the thickness of a water slab that achieves a similar range shift as a specific amount of that material. This concept is useful for computing various range losses of the proton beam while travelling through different materials in the beamline or in the small animal. By using the WET values, all range losses have the same unit, for instance, mm H_2O, enabling straightforward calculations. Zhang and Newhauser have provided a comprehensive formula for the computation of the WET, allowing an accurate enough determination of the water equivalent thickness for a given material [12]:

$$t_w = t_m \frac{\rho_m}{\rho_w} \frac{\bar{S}_m}{\bar{S}_w}, \tag{1.6}$$

where t_w is the water equivalent thickness, t_m the thickness of the material, ρ_m, ρ_w, $\bar{S}_m$, and $\bar{S}_w$ the densities and the mean proton stopping power values of the material and water, respectively. Looking back at the equation of the proton stopping power of a material, this is already calculated relative to the stopping power of water. The equation of the WET can, therefore, be reduced to:

$$t_w = t_m \frac{\rho_m}{\rho_w} RSP. \tag{1.7}$$

Here, the RSP is the relative stopping power as defined in equation 1.2. The concept of the water equivalent thickness is also shown in figure 1.2. As the thickness of the material will vary and is not always known, it is preferable to work with the water equivalent ratio (WER) instead of the absolute thickness. The water equivalent ratio is defined as follows:

$$WER = \frac{t_w}{t_m} = \frac{\rho_m}{\rho_w} RSP \tag{1.8}$$

Note that the WET and WER values are dependent on the energy of the beam and it is thus needed to determine the water equivalency for each setup separately.

1.1.2. Dosimetry

In dosimetry, the absorbed dose of the material is determined [5]. As consistency and reproducibility of treatments are desired, ensuring accurate and uniform dosimetry across various institutions is required. Absolute dosimetry is used to define 1 Gy and to assure that this is equal under different circumstances [13]. This is done by standard laboratories that calibrate their dosimetric measurements with all secondary laboratories in that country. Additionally, cross-calibration is performed between different countries. To minimize the error, the same dosimeter is used. Absolute dosimetry is mostly measured with an ionisation chamber, for instance, an advanced Markus chamber.

Meanwhile, relative dosimetry can be used to measure the physical characteristics of a beam. An advantage is that relative dosimetry can be used in any setup, independent of what is used for the absolute dose measurements. One of the most used relative dosimeters is radiochromic film. This film

gets blackened when irradiated with ionising radiation, which can subsequently be quantified to obtain information on the dosimetry [14].

A more in-depth literature review of dosimetric commissioning methods used in preclinical studies can be found in Appendix B.

1.1.3. Proton Therapy Pre-Clinical Research Workflow

A proton therapy research line starts with conducting a micro-CT scan of a small animal. This CT scan is not only needed for the anatomy of the animal but also to calculate the proton RSPs of the different tissues surrounding the tumour. As discussed in section 1.1.1., the range of the proton beam depends on the stopping power values of the materials it travels through. The proton stopping power values are thus required for a range estimation of the proton beam. This range estimation is used to correctly position the spread-out Bragg peak at the site of the tumour. Such a CT to stopping power calibration is commonly performed in the clinic. However, even though it is similarly useful in pre-clinical research, this is not often done for micro-CT scanners.

A Monte Carlo simulation is performed to simulate the dose distribution of the setup. The stopping power values of the various tissues are used in this simulation with which the range estimation is validated. From this simulation, a treatment plan is made. However, before this plan can be used, a validation needs to take place. Especially in *in vivo* research, it is essential to have the correct dosimetry and correct positioning of the SOBP to be able to mimic the situation in the clinic as closely as possible. After the validation, irradiations can be performed.

A schematic of the proton therapy research line is shown in figure 1.4.

1.2. Biological Response to Proton Therapy

As the primary target of radiotherapy are the tumour cells, the biological response to proton therapy is of significance. To improve earlier diagnostics, understanding its biology is important. Protons can cause cell death by inducing DNA damage. There are two mechanisms through which this DNA damage can be induced: direct and indirect pathways. In the direct pathway, protons entering the cells will interact with the DNA molecules. Because of their high energy, ionisations take place, leading to breaks in the DNA. The cell has different mechanisms to repair DNA damage, however, when not repaired correctly, this can lead to cell death [15]. The induced DNA breaks can either be single-stranded (SSBs) or double-stranded (DSBs), with the latter being more detrimental to the fate of the cell, as their repair is more difficult [16]. Furthermore, protons can cause clustered DNA breaks, due to ionisations occurring close together. Clustered DNA breaks are even more challenging to repair by the DNA repair mechanisms, as accessing the DSBs can be hindered by the close proximity of the breaks [17].

Protons can also indirectly damage cellular DNA. When protons enter the cell, they can interact with water and other molecules within the cells, causing ionisations. This will produce highly reactive free radicals, such as reactive oxygen species (ROS). These free radicals can cause oxidative damage to different cellular processes. ROS can directly interact with DNA and cause breaks or mutations, such as the modification of the base guanine into 8-oxo guanine [18]. These mutations and strand breaks can eventually lead to cell death when not repaired correctly. ROS can cause harm to mitochondrial DNA and proteins, which results in impaired cell function and eventual cell death through apoptosis. [19, 20]. Since protons are charged particles with a greater mass when compared to photons, they tend to generate higher amounts of ROS, particularly in the Bragg peak. Therefore, it is believed that protons induce a stronger cellular response through ROS than photons [21].

An essential concept in the field of radiobiology is Linear Energy Transfer (LET). LET is the amount of energy that is deposited per unit length as ionising radiation traverses a material. It is a measure of how much energy is imparted to the material by ionising radiation. Low-LET radiation deposits its energy over a long distance, while high-LET radiation deposits more energy over a shorter path. Hence, radiation with a higher LET will cause more direct ionisations along its track. Photons are considered low-LET radiation, while the LET of protons varies throughout the Bragg curve, with a significantly higher LET in the Bragg peak [22].

The same amount of absorbed dose can have a different biological effect across various ionising radiation particles because of different patterns in energy deposition [23]. This can be measured in

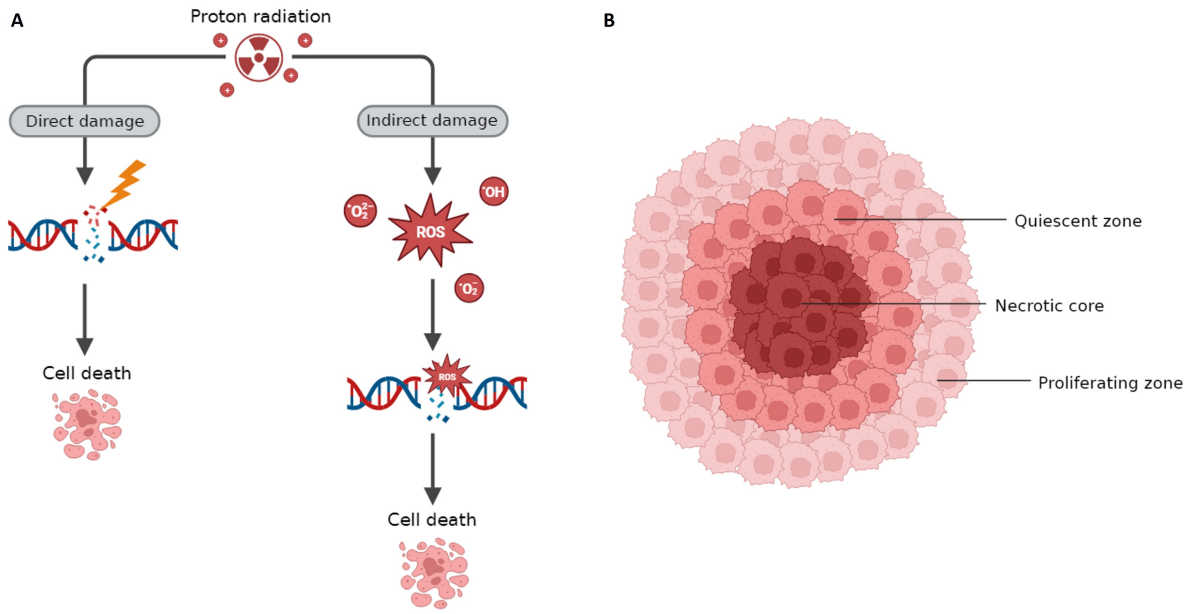

Figure 1.3: (A) Proton irradiation can damage the DNA directly and indirectly. In the direct pathway, the radiation directly causes DNA damage. When this cannot be repaired, it will lead to cell death. In the indirect pathway, protons cause ionisations to water and other molecules, resulting in reactive oxygen species and free radicals. These can cause DNA breaks, resulting in cell death when not repaired. Figure created with Biorender and adapted from [16]. **(B)** A spheroid has three different layers. In the middle, the necrotic core is located, with the quiescent layer surrounding it. The outermost layer consists of proliferating cells. Figure created with Biorender and adapted from [28]

relative biological effectiveness (RBE). The RBE is a scaling factor that is used to compare the biological effect of different particles for the same physical absorbed dose. RBE is defined as follows [23]:

$$RBE = \frac{dose_{reference\ radiation}}{dose_{test\ radiation}}, \tag{1.9}$$

where $dose_{reference\ radiation}$ is the dose of the reference radiation, mostly photon radiation, that produces a certain biological effect, and $dose_{test\ radiation}$ is the dose of the test radiation, in this case of protons, that produces the same biological effect [24]. Protons have a higher RBE than photons, as they are more effective in damaging tumour cells with the same dose than photons [25]. An RBE value of around 1.1 is commonly used for protons [22, 26, 27]. Nonetheless, this value will not always be accurate, as the RBE of protons is dependent on several other factors. A higher LET results in higher RBE values and, conversely, an increase in dose leads to a lower RBE, with a steeper decline of RBE for lower doses. Additionally, the RBE of protons varies with the used biological endpoint [22, 23].

1.2.1. 3D Spheroid Model

Most proton therapy research has been conducted on two-dimensional (2D) cell monolayers. Using 2D cells has many advantages, such as low costs, high reproducibility, and simplicity [29]. However, such a 2D monolayer does not mimic the heterogeneous exposure to oxygen and nutrients and the amounts of signalling molecules that are present in three-dimensional (3D) *in vivo* tumours [30]. The monolayers have a limited amount of neighbouring cells, resulting in reduced cell-cell communication [31]. Additionally, all cells have equal access to oxygen and nutrients, a homogeneity that is not present in its *in vivo* 3D counterpart.

A solution has been introduced in the form of 3D tumour spheroids. Such multicellular 3D spheroids resemble *in vivo* tumours more closely, as they show similar oxygen and nutrient heterogeneities, as well as increased cell-cell interactions compared to the 2D monolayer. Figure 1.3 shows the layered structure of a 3D tumour spheroid. A necrotic core is surrounded by a quiescent zone, where cells have entered a non-dividing, resting state. The outermost layer consists of the proliferating cells.

Spheroids can be formed with or without the use of an extracellular matrix (ECM). Scaffold-free methods include the hanging drop method, where surface tension of the cell suspension and gravi-

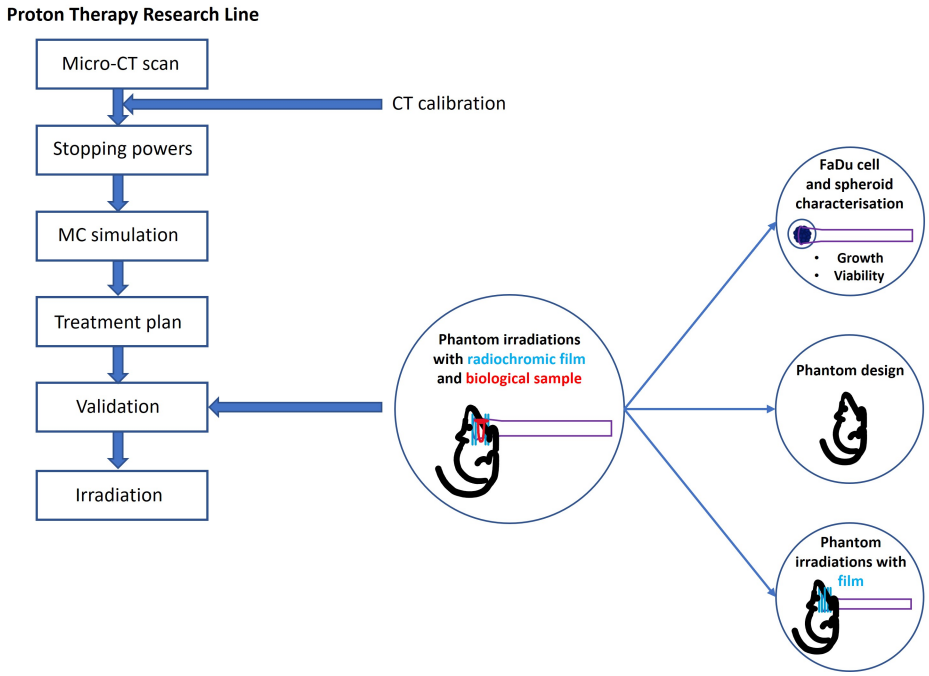

Figure 1.4: An overview of the work that will be addressed in this thesis and its place within proton therapy pre-clinical research

tational force are used to form cell aggregates. Another much-used method is called liquid overlay, where low-adhesive plates are used to prevent cell attachment. By shaking the plate, cell aggregation is facilitated and spheroids are able to form [32]. Alternatively, an ECM, such as Matrigel, can aid the formation of spheroids. Low-attachment plates are utilized in combination with centrifugal forces to gather the cells together and let them form spheroids.

Using a 3D tumour spheroid model will provide a system that is biologically more relevant than a 2D monolayer when investigating dose responses, and will provide better insights into the behaviour of tumours to proton therapy.

1.3. Thesis Outline

To improve current proton therapy, it is essential to closely mimic the clinical setting during pre-clincal research. This means, for example, accurately positioning the Bragg peak in relation to the tumour to minimize dose deposition to healthy tissue. Additionally, biological responses vary along the Bragg curve due to variations in LET and RBE. To attain a comparable response with the clinical response, it is essential to commission the physical side of the proton beam, as well as to validate the biological dose response. This validation step can eliminate various uncertainties during pre-clinical research, hopefully leading to better insights into proton therapy techniques. Therefore, the main objective of this thesis is to dosimetrically and biologically commission a proton therapy research line.

To ensure this accurate dosimetry and positioning even with various tissues along the path of the beam, a phantom is used that geometrically resembles a mouse. The use of such a phantom can be advantageous as it allows for the placement of different dosimeters inside of the phantom. This allows for the validation of the correct dosimetry and positioning before moving on to the actual irradiation of the small animal. Various materials will be used to represent different tissues in the phantom. These materials will be 3D-printed into a phantom that will have slits in the head to place radiochromic film, which will act as the dosimeter. One of the objectives will be to determine which materials are suitable for each tissue to achieve a similar range reduction of the proton beam. Subsequently, the optimal printing settings will be explored, as it has been shown that, for example, a different layer height or orientation can affect the proton stopping power [33, 34]. Next, the phantom with the radiochromic film will be irradiated with the goal to show that it is possible to position the phantom correctly in the SOBP. The dosimeter, the radiochromic film, can be placed at different depths within the phantom, where it

can measure the delivered dose. This enables a validation of the range not only before and after the small animal but also at various positions within.

To validate the biological effects of proton radiation on tumour cells, a 3D tumour spheroid model will be used, made from the FaDu head-and-neck cell line. The dose response of these spheroids will be characterised and compared to the dose response of a 2D monolayer. Ultimately, these spheroids will be placed within the phantom to enable both a biological and a dosimetric validation during proton irradiation.

An overview of all work that will be performed in this thesis is shown in the circles in figure 1.4. The big circle represents the main objective of this thesis and its relevance within the proton therapy research line.

2

Methods

2.1. 2D and 3D Cell Characterisation

2.1.1. Cell Culture

Human-derived FaDu cells (HTB-43, ATCC), epithelial cells of a squamous cell carcinoma from a hypopharyngeal tumour, were cultured in a medium of equal parts Dulbecco's Modified Eagle's Medium (DMEM, Capricorn DMEM-HPSTA) and Ham's F10 (PAN BioTech), with the addition of 10% fetal calf serum (FCS) and 1% penicillin-streptomycin. FaDu cells were passaged twice a week. Phosphate Buffered Saline (PBS, Sigma-Aldrich D8537) was used to wash the cells after which the cells were incubated for 5 minutes at 37°C with Trypsin/EDTA (T3924) to detach the cells. A fraction of the cells were transferred to a new 10 cm culture plate (Greiner Bio-One) with fresh medium. The cells were incubated at 37°C and 5% CO_2.

2.1.2. Cell Irradiations

The day before the irradiations, FaDu cells were trypsinized with Trypsin/EDTA and counted with a cell counter (Countess 3 Invitrogen). 1000 cells were seeded in a 96-well plate (Greiner Bio-One Cellstar) per well. Before the irradiation, all wells with contents were filled entirely with medium or PBS, to allow sealing of the plates using an adhesive sealer (Bio-Rad Microseal MSB-1001) to eliminate the presence of air bubbles. The plates were vertically irradiated with protons at HollandPTC with doses of 2, 4, 6, and 8 Gy in the middle of the SOBP. Figure 2.1 shows a schematic overview of the beamline. A photo of the setup can be found in the Appendix (fig A.1). After the irradiations, the seal and all of the medium were removed and 200 µL fresh medium was added. The cells were incubated at 37°C and 5% CO_2. To check the dose-response, the growth and viability of the cells and spheroids were determined (section 2.1.2-8).

2.1.3. CellTiter-Glo Assay

Seven days after the irradiations, plates containing the irradiated cells were transferred to the Reactor Institute Delft (RID), where a CellTiter-Glo assay (Promega) was performed to determine the viability of the cells. The CellTiter-Glo assay determines the amount of metabolically active cells via a reaction that needs cellular ATP to convert luciferin into oxyluciferin. The luminescent signal of oxyluciferin can be measured with a spectrometer. Half of the medium was removed and an equal volume (100 µL) of CellTiter-Glo reagent was added. After 10 minutes, the contents of the wells were resuspended and transferred to a white 96-well plate (Greiner Bio-One). Luminescence was measured with the Cary Eclipse spectrometer (MY16240001), using an emission slit size of 10 nm and a gate time of 500 ms. The viability of the cells was obtained by normalizing the luminescence levels to those of the unirradiated group.

2.1.4. Spheroid Formation

FaDu cells were trypsinized and counted with a cell counter (Countess). U-bottomed 96-well plates (Greiner Bio-One) were used. These are low-attachment plates, meaning that the cells will not adhere

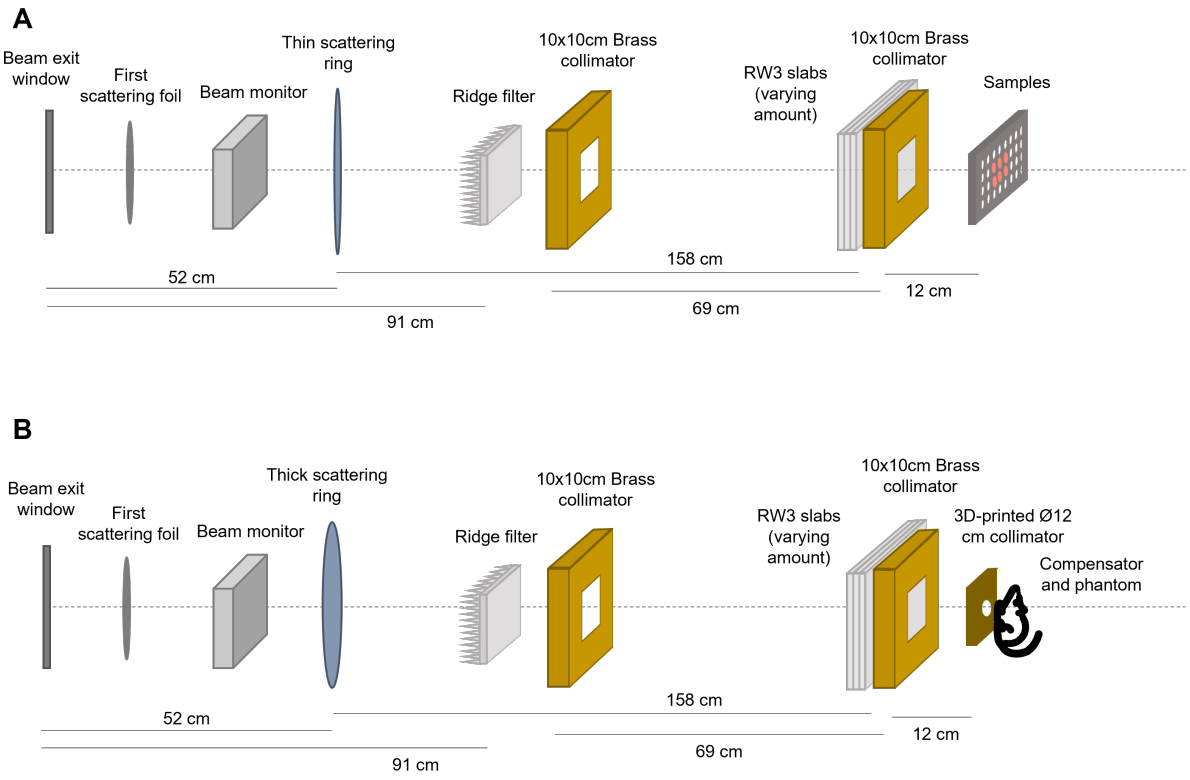

Figure 2.1: A schematic representation of the beamline used for the irradiations at HollandPTC. The proton beam travels to the right. **(A)** Beamline used for cell irradiations. **(B)** Beamline used for phantom irradiations

to the bottom of the well and are, therefore, able to form aggregates with each other. At the RID, 2000 cells per well were seeded together with 1% Matrigel (Corning Matrigel Matrix) in cold medium (< 10°C). Matrigel is composed of various extracellular matrix proteins that are specific to the tumour microenvironment, such as laminin [35], and was used as the matrix for the spheroids. The plates were spun down using the Eppendorf centrifuge at 1000 rpm for 10 minutes at 10 °C. The plates were incubated at 37 °C and 5 % CO_2 and were left undisturbed for at least 4 days in order for stable spheroids to form.

2.1.5. Spheroid Irradiations

The spheroids were irradiated seven days after the formation. The spheroids were divided into four different U-bottomed 96-well plates: one control plate and three plates for the different doses. The plates were transferred from the RID to HollandPTC for irradiation. The wells were filled entirely with medium and sealed with BioSeal. The plates were vertically irradiated with protons at HollandPTC with doses of 4, 6, and 8 Gy. The schematic beamline can be seen in figure 2.1. Afterwards, the seal and half of the medium were removed and 100 µL fresh medium was added to each well. The spheroids were incubated at 37 °C and 5 % CO_2.

2.1.6. Spheroid Growth Measurements

After seven days, the spheroids were transferred back to the RID. Spheroids were imaged at different time points with a Gapel microscope (S245B) and an attached camera at one of the eyepieces. A 3x magnification was used. Glass beads of known sizes were imaged and analysed to determine the pixel-to-micrometre scale. The diameter and area of the spheroids were measured using the Fiji ImageJ software. Relative growth was determined by normalising the growth per spheroid at the last time point to the control group. A Kruskal-Wallis test was performed to statistically measure the difference between the groups.

2.1.7. CellTiter-Glo 3D Assay

The viability of the spheroids was determined thirteen days after the irradiations with the CellTiter-Glo 3D assay. This assay is equal to that described in section 2.1.3, however, the reagent is designed with an increased lytic activity to be able to penetrate the whole spheroid. Half of the medium was removed and an equal volume (100 µL) of reagent was added to each well. The plates were incubated at room temperature for 20 minutes. Afterwards, the contents of the wells were resuspended to help the reagent to reach the inner parts of the spheroids as well. The spheroids were incubated for another 20 minutes, after which the contents were resuspended again and transferred to a white 96-well plate. The luminescence was measured with the Cary Eclipse spectrometer. A 10 nm emission slit size and a gate time of 500 ms was used. The viability of the spheroids was obtained by normalizing the luminescence levels of the irradiated spheroids to the values of the unirradiated group.

2.1.8. Live/Dead Staining

To get an idea of the size of the necrotic core in the spheroids irradiated with different doses, live/dead staining was performed. Calcein acetoxymethyl ester (calcein AM) is used to stain live cells. It can cross the cell membrane via passive transport and is hydrolyzed in the cytosol by an esterase to the green-fluorescent molecule calcein. This molecule is retained in cells with intact cell membranes only. The necrotic cells are stained with propidium iodide (PI), as this molecule can only enter cells with a compromised membrane. It then binds to nucleic acid within the cell and, therefore, stains the nucleus of a necrotic cell.

From each group, six spheroids were transferred to a new U-bottomed 96-well plate. They were moved from the RID to the Erasmus MC. Thirteen days after irradiations a live/dead staining was performed. The propidium iodide was diluted to 1:500 in medium and the calcein AM to 1:800. The spheroids were washed with PBS and the propidium iodide solution was added. The spheroids were incubated at 37 °C and 5 % CO_2 for 5 hours and 45 minutes. Next, the calcein AM solution was added and the spheroids were incubated for another 15 minutes. The spheroids were transferred to a flat-bottomed 96-well plate and washed with PBS. Per condition, two spheroids were imaged with the confocal microscope. Three spheroids per condition were imaged with the widefield Olympus IX-70 microscope.

The images were analysed with the Fiji ImageJ software. The colour brightness was adapted and a threshold was set for both the PI signal and the Calcein AM signal. The area was measured for both signals and the ratio between the necrotic cells and the viable cells was determined.

2.2. Phantom

2.2.1. Phantom Design

The phantom used in this thesis is murine-based, meaning that it is geometrically similar to a mouse. To that end, the MOBY phantom was used, a model with detailed anatomical structures of a laboratory mouse. As this phantom was made with only one material, only the rendering of the outside of the MOBY phantom was used and not all the structures inside. The phantom was divided into five different slices of equal thicknesses (2.1 mm) that were held together by two pins in the middle of the phantom. The first and last slices of the phantom had varying thicknesses, depending on the shape of the mouse model. A slot of 0.4 mm was left in between for easy placement of the EBT3 radiochromic film. A spherical tumour was placed in the neck of the phantom, with a diameter of 5 mm. However, because this version of the phantom is printed with only one material, this tumour is strictly fictive. A structure to easily mount and align the phantom with the rest of the beamline was also designed. A collimator with a diameter of 12 mm was attached to this structure in such a way that it aligned with the tumour inside of the phantom. The design of the phantom and additional structures was made using the software Slicer. The design was made by Ernst van der Wal at HollandPTC.

2.2.2. Compensator Design

To ensure a uniform dose to the whole tumour, a compensator is needed, as there are varying amounts of tissues with different stopping power values in front of the tumour. This compensator will, therefore, be specific per mouse. To that end, a Python script was made to calculate the amount of water equivalency that is in front of the tumour for each voxel, making use of a CT scan of the mouse. The shape of the compensator will then be the inverse of these water equivalency values. This mouse-specific com-

Block	Material	Colour	Layer Height	Infill	Rotation
1.1	PLA	Oh My Gold	0.1 mm	Rectangular	0 °
1.2	PLA	Oh My Gold	0.1 mm	Rectangular	90 °
1.3	PLA	Oh My Gold	0.2 mm	Rectangular	0 °
1.4	PLA	Oh My Gold	0.05 mm	Rectangular	0 °
1.5	PLA	Oh My Gold	0.1 mm	Concentric	0 °
2.1	PLA	Grey	0.1 mm	Rectangular	0 °
2.2	PLA	Blue	0.1 mm	Rectangular	0 °
2.3	ASA	-	0.1 mm	Rectangular	0 °

Table 2.1: Printing settings for the different 3D-printed blocks. The blocks were printed with the Prusa 3D printer at HollandPTC

pensator can then be 3D printed. A flowchart of that code can be found in appendix D. However, the phantom used during this project was made of only one material. The compensator for this phantom will, therefore, simply be the inverse of the shape of the front of the mouse. The compensator is made such that the minimum thickness of material before the first EBT3 film is 17.5 mm, while without the compensator this thickness varies between 2.87 mm and 4.07 mm. The compensator was incorporated into the mount of the phantom, ensuring an accurate alignment with the phantom in the beamline.

2.2.3. Influence of Different Printing Settings

To investigate the influence of varying printing settings on the WET and density of different materials, blocks of 3 x 3 x 1 cm were printed with varying layer heights, infill, colours, and materials. The used settings are shown in table 2.1. CT scans of the blocks were made with the VECTor micro-CT scanner from MILabs at the ErasmusMC. A tube voltage of 50 kV, a tube current of 170 µA, 75 ms exposure time, and a 0.5 mm Al filter were used. The CT images were reconstructed using a voxel size of 72 µm with a Hann projection filter. To reduce the amount of noise, a 3D median filter ($\sigma_{x,y,z} = 2$ pixels) and a 3D Gaussian filter ($\sigma_{x,y,z} = 2$ pixels) were applied to the reconstructed images. The CT number of a block was obtained by taking the middle slice of the CT scan and averaging over the whole square. The CT to stopping power calibration was applied to the reconstructed images, as described in appendix C. From this, the density, stopping power value, and water equivalent ratio were determined for all blocks. In Appendix D a flowchart of the written and used code can be found. The theoretical HU value and RSP of the PLA filament before printing was calculated using the given density of 1.24 g/cm^3 and the elemental composition (H: 5.59, C: 54.76, O: 44.99) [36]. HU was calculated with:

$$HU = \left(\frac{\overline{\mu}}{\overline{\mu}_{H_2O}} - 1 \right) * 1000, \tag{2.1}$$

where

$$\frac{\overline{\mu}}{\overline{\mu}_{H_2O}} = \frac{\rho}{\rho_{H_2O}} \frac{\sum_{i=1}^{n} (w_i/A_i)(Z_i + Z_i^{2.86} k_1 + Z_i^{4.62} k_2)}{(w_H/A_H)(1 + k_1 + k_2) + (w_O/A_O)(8 + 8^{2.86} k_1 + 8^{4.62} k_2)}, \tag{2.2}$$

and the RSP with equation 1.2.

Additionally, the water equivalent ratio was determined experimentally determined using the CUBE within the beamline at HollandPTC. The obtained dose depth curve was compared to the dose depth curve of water, which resulted in a shift of the peak. The water equivalent ratio was calculated for all the different blocks from this range shift.

2.2.4. 3D Printing

The phantom and additional structures were printed with the Prusa 3D printer (MK3S) at HollandPTC by Ernst van der Wal. For the phantom the material Polylactic Acid (Prusament PLA/PLA by Prusa Polymers) in the colour ”oh my gold” was used. It was printed with a 0.4mm nozzle, and 0.1 mm layer height. A rectilinear way with a 100% infill was used. The PLA filaments had a density of 1.24 g/cm^3 before 3D printing. The compensator, as well as the mount, were printed using the same material and settings as the phantom. The collimator was printed with ColorFabb CopperFill, PLA filaments with high amounts of copper particles. This material had a density of 4.0 g/cm^3. The collimator was printed with a 0.1 mm layer height, in a rectilinear manner with 100% infill.

2.2.5. Phantom Irradiations

The phantom was mounted in the beamline as shown schematically in figure 2.1. EBT3 Gafchromic film was cut in squares of around 7 x 7 cm. Per experiment, six or seven pieces of film were placed within the phantom and on both outsides of the phantom. For the irradiations, a different position within the Bragg peak was reached by changing the amount of RW3 slabs in front of the phantom. RW3 slabs are plates of polystyrene with a density of 1.045 g/cm^3. To show that the positioning of the phantom in the Bragg peak was as desired, the tumour was either irradiated in the centre of the plateau of the SOBP or at the distal end of the plateau. The amount of RW3 slabs that were placed within the beamline was calculated using the WER of the RW3 slabs (0.96), of PLA (1.13), and of EBT3 film (0.358), and the measured dose depth curve, using the following formula:

$$RW3\,(mm) = \frac{position\,(mm) - (PLA_{infront}\,(mm) * 1.13) - (films * 0.358)}{0.96}, \tag{2.3}$$

where the $position$ is the desired position within the Bragg peak in mm, the $PLA_{infront}$ is the amount of material that is already in front of that slice, and $films$ is the number of films that are in front. Irradiations were carried out using a dose rate of 1.33 Gy/min. A dose of approximately 2 Gy was given to the phantom.

Three versions of the same phantom were also 3D-printed with a hole that could fit a pinpoint detector. The holes of these phantoms were placed directly at the start, the centre, and the end of the tumour, corresponding to the first three film positions. These phantoms were irradiated in turn to obtain absolute dose measurements at different positions within the phantom. The pinpoint measures a volume of 0.016 cm^3.

2.2.6. Film Analysis

EBT3 Gafchromic film was irradiated with various doses, using the same beamline as the phantom irradiations. The film pieces were scanned with the EPSON Expression 12000XL scanner and converted with the Epson 2 scan software to 300 dpi, 48-bit colour images. Using Fiji ImageJ, the average grey value of each irradiated film was determined and a grey value-to-dose calibration was obtained.

The irradiated film pieces from the phantom were removed, scanned, and converted to 300 dpi, 48-bit colour images. The films were analysed using Fiji ImageJ. The grey value-to-dose calibration was applied to all films. A rectangle of 400 by 20 pixels was drawn in both x- and y-direction and placed in the middle of the tumour. The profile of this line was plotted. Additionally, a square of 100 by 100 pixels was drawn on the background of the film. Of this square, the profile was plotted and averaged. This average was subtracted from the x- and y-direction line plots. Next, for each film, the measured dose within the tumour was calculated by averaging the dose obtained from the line plots in that region. The tumour was defined as the circle with a diameter of 5 mm in the middle of the irradiated area that was visible on the film, as the collimator was slightly bigger than the tumour, and, therefore, also surrounding parts were irradiated. For each set of films, the relative dose of a film was calculated by finding the highest average dose within the tumour of all films in that set and dividing the average dose within the tumour of a film by this maximum value. The dose delivered to the surrounding material was calculated by subtracting the total dose deposited within the tumour from the total dose of the whole irradiated area. Additionally, the uniformity of the line profile plots was determined for the middle 5 mm of all films.

The systematic error of the film analysis was obtained by combining the intra-personal, inter-personal, and calibration error, as the results of the analysis depend on multiple factors. For the intra-personal error, the same films were analysed multiple times by the same person, on the same computer. Additionally, the films were analysed on different computers, the error of which was also taken into account. The interpersonal error was obtained by comparing the analysis made by different persons. This reanalysis data was given by Marta Rovituso. For the calibration error, a new calibration was made, with which the films were reanalysed.

2.2.7. Dose Depth Measurements

The dose depth curve of this beamline was measured using an advanced Markus chamber. The Markus chamber measures a volume of $0.02cm^3$ in the middle of the beam. The beamline as depicted in figure 2.1 was used, replacing the phantom with the Markus chamber. The 3D-printed collimator was attached

in line with the beam to the front of the Markus chamber. The number of RW3 slabs in front of the Markus chamber was changed from 5 mm up to 101 mm to obtain a dose depth curve.

Relative measurements of the dose depth curve were performed by placing 12 12 x 12 cm square pieces of EBT3 Gafchromic film at different places in between the RW3 slabs. The slabs with the films were placed at the site of the phantom in figure 2.1, with the 3D printed collimator attached to the first RW3 slab, in alignment with the beam. A dose of 2.5 Gy was given. The films were removed, scanned, and converted to 300 dpi, 48-bit colour images. The films were analysed with Fiji ImageJ. The grey value-to-dose calibration was applied to all films. A rectangle of 400 by 20 pixels was drawn and placed in the middle of the films. The line profile was plotted and the average dose was determined. This was done for both the x- and y-direction. Additionally, the relative dose of all films was determined as described in section 2.2.6.

Furthermore, individual slices of the phantom were irradiated with a Markus chamber behind the slices. After each irradiation, the next slice was added and irradiated again.

3

Results

3.1. 2D and 3D Cell Characterisation

3D spheroids are thought to better represent a tumour because of similar heterogeneities and cell-cell interactions. However, there is still a limited understanding of how such spheroids respond to proton therapy. To that end, this thesis aims to characterize their dose response and compare the response of spheroids to that of cells. While clonogenic survival curves are typically used to determine the dose response, such experiments are challenging to perform with spheroids. Therefore, the viability, based on the metabolic activity of the cells and spheroids, is chosen as the biological endpoint.

To determine the presence of a dose-dependent difference in the growth rate of the FaDu spheroids, the diameter was measured over time to obtain the growth of the spheroids (fig. 3.1A). The spheroids had an average diameter of 500 μm on the day of irradiation, seven days after their formation. The control group, as well as the group irradiated with 4 Gy, grew to a size of around 700 μm a week after the irradiation, while the spheroids treated with 6 and 8 Gy only grew to a size of 600 μm. After the first week, they did not grow much further, even a slight decrease can be observed in the growth of the spheroids irradiated with 8 Gy. The diameters of the spheroids 13 days post-irradiation were normalized to the control group (fig. 3.1B). No significant difference in the size 13 days post-irradiation was found between the unirradiated group and the group irradiated with 4 Gy; a decrease of only 3% was shown. Nonetheless, there was a significant difference between the control and 6 Gy groups (p=0.0269) found by the Kruskal-Wallis test. The growth after 13 days showed a decrease of 11% compared to the control group. Additionally, a significant difference was found between the growth of the control and 8 Gy groups as well, with a decrease of 18% (p=0.0004). Figure 3.1C shows microscopic images of representative spheroids from each group over time. Surrounding the 8 Gy irradiated spheroids, a lot of detached, single cells can be seen on day 13. To a lesser extent, this can also be observed around the spheroids that received a lower dose. Furthermore, the spheroids stayed fairly round, independent of the delivered dose.

To compare the dose-response of the 2D monolayer and the 3D spheroids, the viability was determined for different given doses (fig 3.1D). The viability was normalized to the control group, such that the unirradiated cells had a viability of 100%. A dose-dependent curve was observed, where at 8 Gy the viability declined to 5.4%. The viability was reduced by 50.6% on average compared to each step of 2 Gy lower. For the 3D spheroids, the viability looked quite unlike the curve of the cells. The viability of the 4 Gy irradiated group was 10.9% higher than the control group, while the 6 Gy irradiated group had a viability that was approximately similar to the control group, with a decrease of only 0.7%. The group irradiated with 8 Gy did show the lowest viability, however, a viability of 82.6% and a decrease of only 17.1% compared to the control group was found. In the supplementary figures, the standard error of the measurements of the viability assay is shown (fig. A.2). The measurements of the spheroids showed a large variation, especially when compared to the measurements of the cells.

To gain a better understanding of why the spheroids did not show a similar dose-dependent viability curve, a Calcein-AM/PI live/dead staining was performed. Representative microscopic images taken with a widefield fluorescence microscope and a confocal microscope are shown in figure 3.1E. Here,

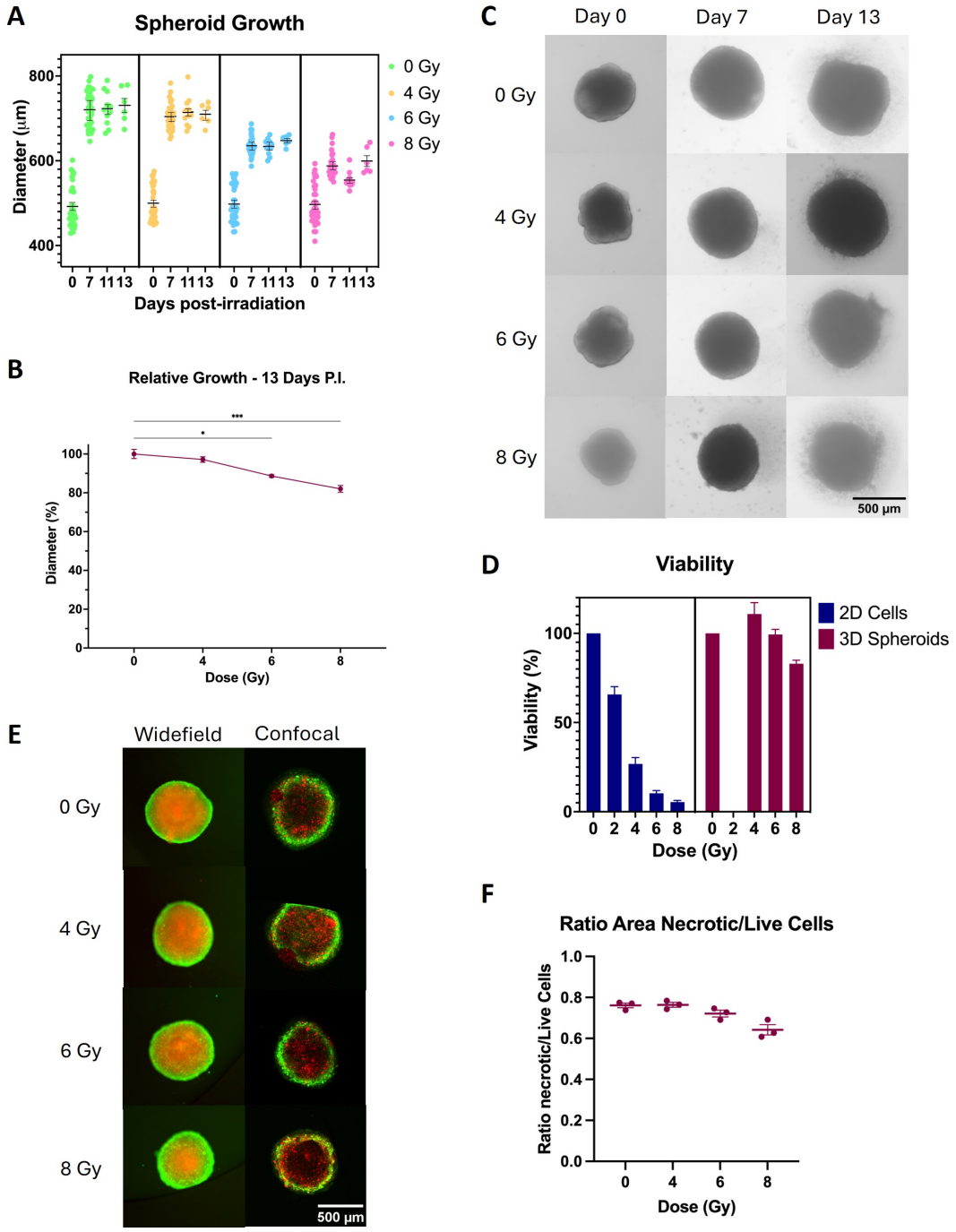

Figure 3.1: 2D and 3D cell characterisation **(A)** Diameter (μm) measured at different timepoints post-irradiation (n=3). Each experiment had 12 spheroids per group, at day 13 6 spheroids per group. **(B)** The size of the spheroids 13 days post-irradiation is normalized to the unirradiated spheroids, giving the relative growth for different delivered doses. The Kruskal-Wallis test gave siginifant values between 0 Gy 6 Gy and 0 Gy - 8 Gy. * p<0.0332, ** p<0.0021, *** p<0.0002, **** p<0.0001. **(C)** Microscopic images of a representative spheroid are shown. **(D)** The viability of the cells in a 2D monolayer and in a 3D spheroid was determined with the CellTiter-Glo assay (n=3, 6 measurements per experiment). Viability is normalized to the control group. The assay is performed 7 days p.i for the cells and 13 days p.i. for the spheroids. **(E)** Representative widefield and confocal images of spheroids with live/dead staining. Necrotic cells are stained red, live cells green. **(F)** From the widefield images the area of necrotic cells and that of the live cells is measured and the ratio between the two is determined

the necrotic cells are represented in red and the live cells in green. The live cells were located more towards the edges of the spheroids. From the widefield images, the ratio between the necrotic cells and the live cells was determined for three spheroids of each group (fig. 3.1F). The ratio between the necrotic cells and the live cells of the unirradiated spheroids was determined to be 0.90. Apart from the spheroids that received 8 Gy with a ratio of 0.86, the groups did not show major differences.

3.2. Phantom Design

The phantom needs to be geometrically similar to a mouse, to be able to use it for range validation during preclinical research. To that end, the MOBY phantom was adapted such that radiochromic film could be placed within the phantom at different set positions (fig. 3.2A). Between all films, 2.1 mm of material is located and slits of 0.4 mm were made in between for the film placement. A compensator was added before the phantom along the line of the fictive tumour (in the head-and-neck region). This compensator was mounted to the phantom to ensure correct alignment. Photos of the 3D-printed phantom can be seen in figures 3.2B (from the side) and C (from the top).

In order to validate the range of the phantom, some range reduction information similar to that of the tissues needs to be incorporated into the phantom. To that end, the phantom needs to be printed with materials with a similar stopping power to that of the different tissues within the mouse. Different materials were available, the stopping power of three of which was determined in this thesis. As some papers suggest that different printing settings affect the stopping power of the printed object [33], blocks with different printing settings (table 2.1) were printed and scanned with a micro-CT scanner (fig. 3.2D. Some air pockets can be seen, mainly around the inside of the edges of the block. Not many visible differences were observed in the CT scans between the different layer heights (1.1, 1.3, 1.4). A difference in how the layers were printed can be seen when a concentric infill was used (1.5) instead of a rectilinear infill (1.1). No visible difference was observed in the CT scans between the different colours (1.1, 2.1, 2.2). Yet, block 2.3, printed with acrylonitrile styrene acrylate (ASA), seemed slightly darker on the CT scan whne compared to PLA (1.1). Block 2.1 was not printed with the correct infill, as can be seen on the CT scan. This was also clear when looking at the relative stopping powers, determined using the CT-to-stopping power calibration on the CT scans (fig. 3.2E). As it is mostly filled with air, the RSP is fairly low and the standard deviation high. The other PLA blocks of that colour all had a density and stopping power slightly higher than 1. The block printed with ASA (2.3), had a lower density and stopping power compared to the others, as well as the blue PLA block (2.2). The mean HU values and respective calculated stopping powers are listed in table 3.1.

For the determination of the range reduction of the phantom, the water equivalent ratio of all materials used in the beamline is required. The water equivalency of the material used for the phantom (PLA) was determined to be 1.11, and that of the RW3 slabs to be 1.05.

Block	Mean HU	RSP
1.1	7 $\pm$ 32	1.0401186
1.2	-12 $\pm$ 37	1.0139674
1.3	-21 $\pm$ 31	1.0139674
1.4	5 $\pm$ 35	1.0356337
1.5	-1 $\pm$ 42	1.0223243
2.1	-767 $\pm$ 318	0.3135992
2.2	45 $\pm$ 31	0.9974976
2.3	-229 $\pm$ 26	0.9254154

Table 3.1: The mean HU ($\pm$ std deviation) was determined using ImageJ by averaging the grey values of the middle slice of the CT scan. The relative stopping power (RSP) values of the blocks printed with different settings were calculated from the CT scans. The corresponding settings can be found in table 2.1. Block 2.1 was incorrectly printed with a low infill

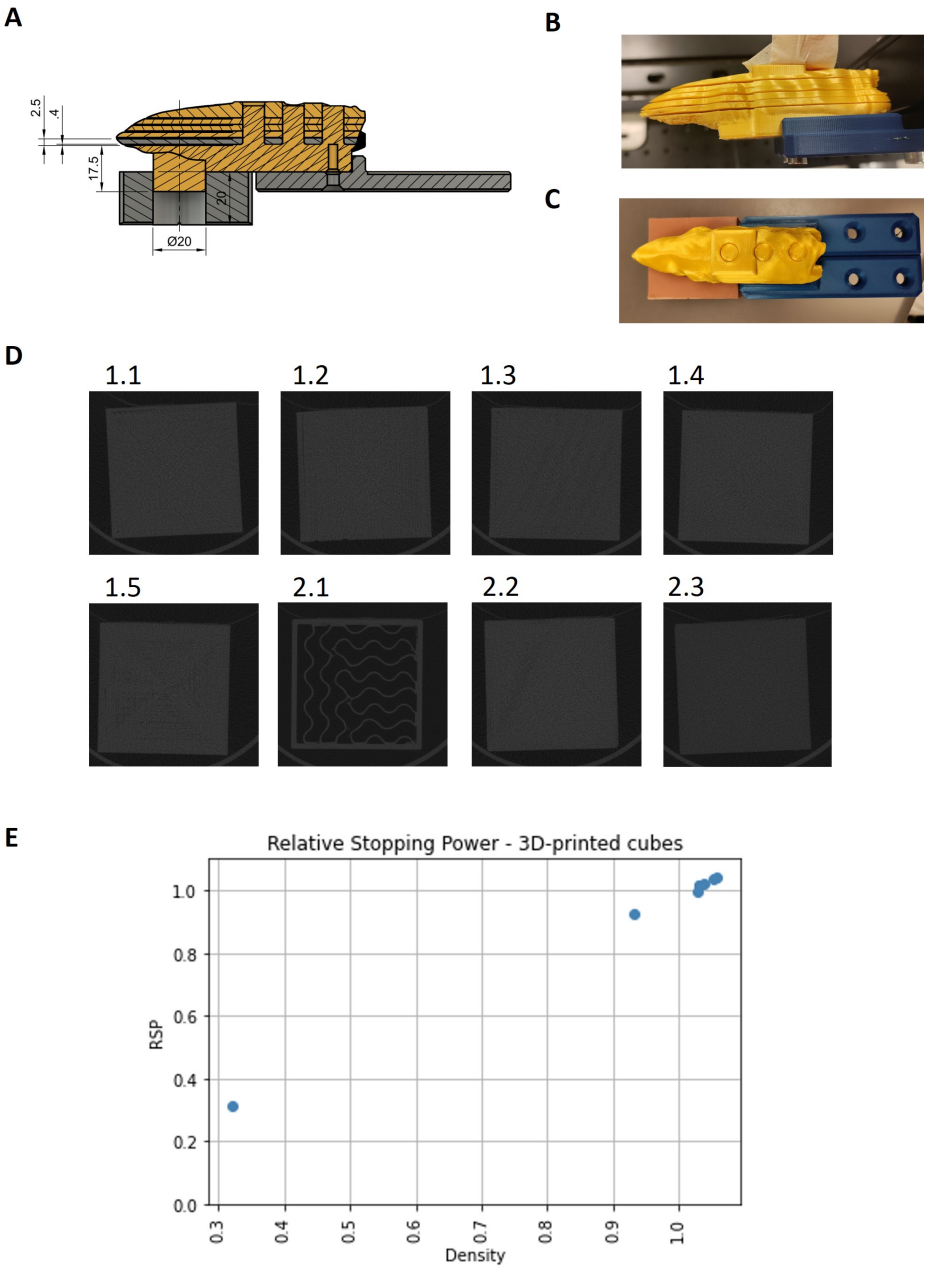

Figure 3.2: Phantom design **(A)** A schematic drawing of the phantom with the compensator and mount. The sizes between the slits are 2.1 mm. Created by Ernst van der Wal. **(B)** A photo of the printed phantom from the side without the compensator. **(C)** A photo of the phantom from the top. Below, in brown, the 3D-printed collimator can be seen, and in blue is the mount. **D** Middle slice of the CT scan of the printed blocks. The numbers correspond to different printing settings, which can be found in table 2.1. Block 2.1 was printed with a too low infill. The post-reconstructed images can be found in the appendix (fig. A.8). **E** The relative stopping power, calculated using the CT calibration and the CT scans of the blocks, plotted against the density of the blocs, also obtained from the calibration

3.3. Phantom Irradiations

To ensure accurate dose delivery and proper positioning of the phantom, radiochromic EBT3 film was used as a dosimeter at various points within the phantom (fig. 3.3A). Six pieces of EBT3 film were placed within the phantom of which the first at the start of the tumour, the second in the centre, and the third at the end of the tumour. The fourth and fifth films were positioned at equal distances further within the phantom. Finally, the sixth film was placed directly outside of the phantom.

First, 81 mm of RW3 slabs were placed in front of the phantom, such that the last point of the tumour still received 98% dose, while ensuring that less dose was deposited to the rest of the tissues. No compensator was used for the first experiment. Line profiles were taken from the scanned film as shown by the red and blue lines (fig. 3.3B). The profile plots from the grey values are shown in the supplementary figures (fig A.4). The applied exponential grey value-to-dose calibration was of the form $y = 0.015266 * e^{0.00013034x}$ (fig. A.5). The dose profile plots (fig. 3.3C) showed similar results in the x- and y-direction, except for the last film, which was placed behind the phantom. For all films, slightly curved profiles were observed. This is reflected in the uniformity of the films, which is 97% for the first film, but only 91 and 70% for the last two films, respectively (table 3.2B). It can be seen that the collimator is bigger than just the tumour, the borders of which are indicated by the grey vertical lines. The highest dose was deposited in the first film, afterwards the dose decreased gradually. The average dose per film was determined at the site of the tumour (fig. 3.3D). The dose already decreased within the tumour, leading to an intra-tumour variation of 22% (table 3.2A). This variation could also be seen when the normalised dose values were placed within the measured Bragg curve with this setup (fig. 3.3E), where the first three points did not all align with the Bragg curve.

Subsequently, the compensator was added and the number of RW3 slabs was adjusted to 72 mm, ensuring equal positioning of the phantom. The addition of the compensator led to more flattened line profiles in both directions (fig. 3.3F). The first three films showed comparable doses, while the last two were evidently lower. It should be noted that films 3 and 4 were likely swapped during their placement. In this graph this was corrected by switching them back, however, it was not completely certain that they were actually swapped during the experiment. It should be noted as well that there was no usable data obtained from the last film. The scan of this film was compromised when opened in the analysis software in such a way that it could not produce reliable results. The data was, therefore, excluded from the rest of the analysis. The average doses (fig. 3.3G) showed a low intra-tumour variation of only 1.1%. After the tumour, the average dose deposition was reduced almost linearly. The shape of the dose-depth profile corresponds to the end of an SOBP. Nonetheless, when placed in the Bragg peak (fig, 3.3H), the alignment was not accurate and seemed to have been shifted slightly to the right.

Ultimately, the phantom was placed in the middle of the SOBP by leaving only 58 mm of RW3 slabs. The compensator was still present, as can be seen by the flatter line profiles (fig. 3.3I). The uniformity was again quite high, all films showed a uniformity of around 96-98%. Similar profiles were observed across all films. However, film 4 showed a slightly higher profile than the other films. It should again be noted that there was no data from film 5 because of a compromised scan. The same pattern was observed in the dose-depth plot (fig. 3.3J). A maximum variation of 7.6% and an intra-tumour variation of 2.9% was found. The normalised dose values did not align well with the measured Bragg curve (fig. 3.3K), as the fourth point had a much higher dose value. The Bragg curve with the normalised data points from reanalysed data can be found in the supplementary figures (fig. A.6).

The systematic error of the film analysis stemmed from various sources. The intra-personal error, accounting for human variability during the analysis, was computed to be 1.392%. Furthermore, conducting the analysis on a different computer, even by the same person, yielded an error of 2.928%. As a person may be biased towards specific results, an interpersonal error needed to be included as well. The error between the analysis performed by separate persons appeared to be 2.708%. Lastly, the calibration also contributed to the systematic error. Recalibrating and reanalysing the films led to a 9.473% error. Collectively, these contributions reached a total systematic error of 9.981%, or 3.145% when the calibration error was excluded. A comparison of a reanalysis of one of the sets of film can be found in the supplementary figures (fig. A.7).

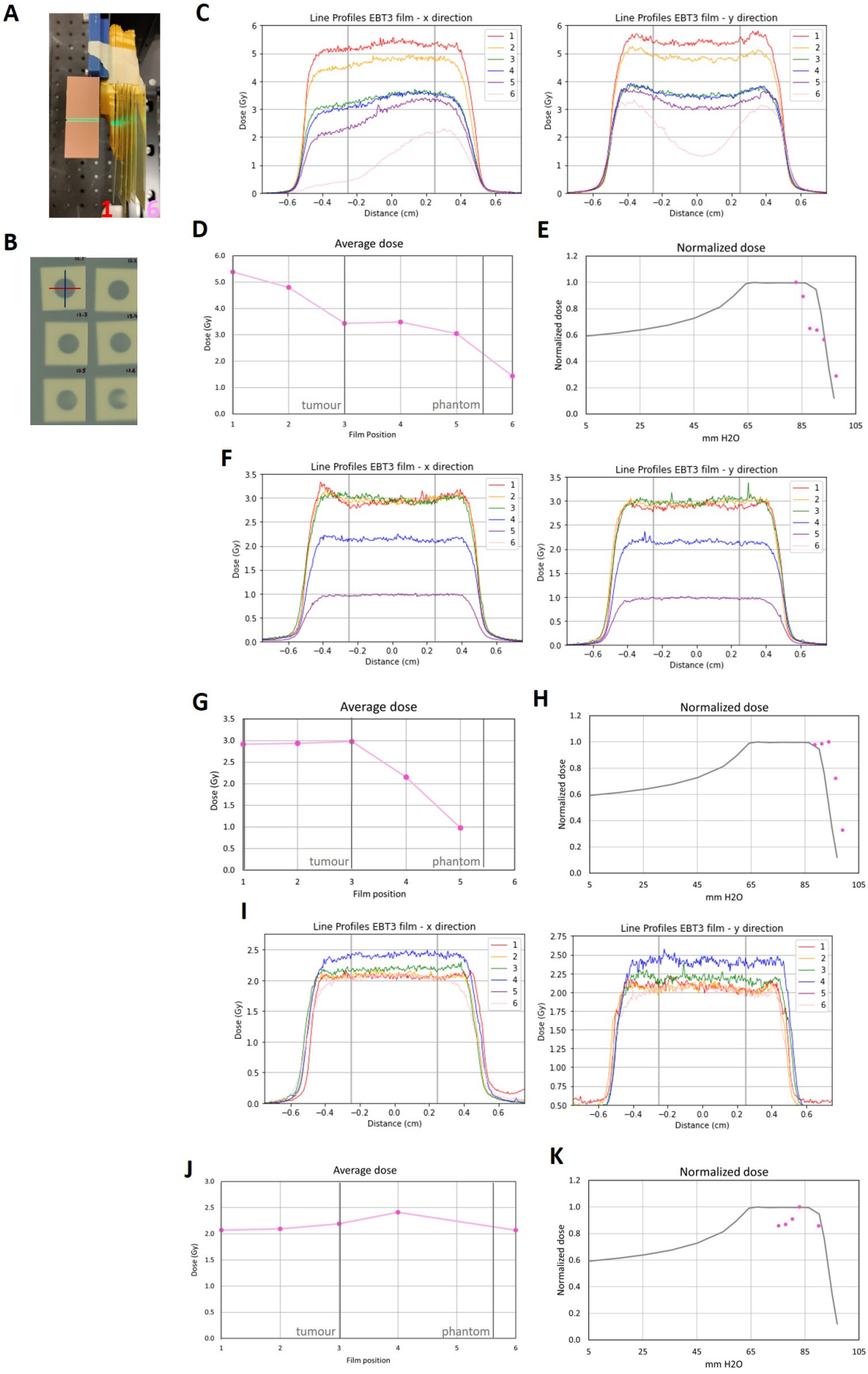
A
1
6
B
C
Line Profiles EBT3 film - x direction
Line Profiles EBT3 film - y direction
Dose (Gy)
Distance (cm)
1
2
3
4
5
6
D
Average dose
tumour
phantom
Film Position
E
Normalized dose
Normalized dose
mm H2O
F
Line Profiles EBT3 film - x direction
Line Profiles EBT3 film - y direction
G
Average dose
tumour
phantom
Film position
H
Normalized dose
I
Line Profiles EBT3 film - x direction
Line Profiles EBT3 film - y direction
J
Average dose
tumour
phantom
Film position
K
Normalized dose

Figure 3.3: Phantom Irradiations **(A)** A photo of the phantom (yellow) when mounted in the setup for the irradiation. The brown block is the 3D-printed collimator. Six pieces of EBT3 film are placed within the phantom, numbered 1 to 6. The green line is the beamline, which comes in from the left. **(B)** The radiochromic film after irradiation and scanning. Darker discolouration means a higher deposited dose. The blue line illustrates the line profile taken in the y-direction and the red on the line profile in the x-direction. **(C)** Line profiles of the irradiated film in both x- and y-direction. No compensator was used. There is 81 mm of RW3 slabs in front, placing the phantom at the end of the SOBP. The tumour is located between the grey vertical lines. **(D)** The dose from the line profiles from c was averaged for each film within the location of the tumour (i.e. between the grey lines in the line profile plots). The location of the tumour and the rest of the phantom is depicted in the figure. **(E)** The average dose values from d (pink dots) are normalised to 1 and plotted together with the Bragg curve measured with the Markus chamber (grey line). **(F)** Line profiles of the irradiated film in both x- and y-direction. A compensator was used. There is 72 mm of RW3 slabs in front, placing the phantom at the end of the SOBP. The tumour is located between the grey vertical lines. **(G)** The dose from the line profiles from f was averaged for each film within the location of the tumour. The location of the tumour and the rest of the phantom is depicted in the figure. **(H)** The average dose values from g (pink dots) are normalised to 1 and plotted together with the Bragg curve measured with the Markus chamber (grey line). **(I)** Line profiles of the irradiated film in both x- and y-direction. A compensator was used. There is 58 mm of RW3 slabs in front, placing the phantom in the middle of the SOBP. The tumour is located between the grey vertical lines. **(J)** The dose from the line profiles from i was averaged for each film within the location of the tumour. The location of the tumour and the rest of the phantom is depicted in the figure. **(K)** The average dose values from j (pink dots) are normalised to 1 and plotted together with the Bragg curve measured with the Markus chamber (grey line)

(a)

	3.2c	**3.2f**	**3.2i**
Maximum variation	57.8%	50.6%	7.6%
Variation in phantom	27.7%	50.6%	7.6%
Variation in tumour	22.1%	1.1%	2.9%

(b)

Film	**3.2c**	**3.2f**	**3.2i**
1	97.1%	97.2%	97.3%
2	97.4%	97.2%	95.8%
3	95.3%	96.4%	97.3%
4	95.1%	96.4%	97.7%
5	91.9%	97.1%	-
6	70.8%	-	97.6%

Table 3.2: Variation and uniformity of the line profiles. **(A)** The variation between the different films. The maximum variation is between all films, the variation in the phantom between the films placed in the phantom (films 1-5), and the variation in the tumour is only between the films in the tumour (films 1-3). It is calculated for figure 3.3a, c, and f. **(B)** Uniformity of the different films. The uniformity is calculated for the middle 5 mm of the line profile only

As the film measurements within the phantom did not align well with the Bragg curve measurements performed with the Markus chamber, dose depth measurements with EBT3 film were performed as well (fig. 3.4A). The shape of the 3D collimator was clearly visible in the scans of the film. It can be seen that in the first five films, the collimator did not stop all protons. The normalised dose values (red dots) were plotted together with the Bragg curve obtained with the Markus chamber (blue line, fig. 3.4B). At the entrance of the Bragg curve, the film measurements did not align well with the Bragg curve, and a large variation was observed. In the SOBP and the distal fall-off region, the few measurements were slightly better aligned.

Next, the dose was measured with a Markus chamber after each slice of the phantom (fig. 3.4C). These normalised values were nicely aligned with the Bragg curve. Lastly, pinpoint measurements within the phantom also aligned well with the Bragg curve (fig. 3.4D).

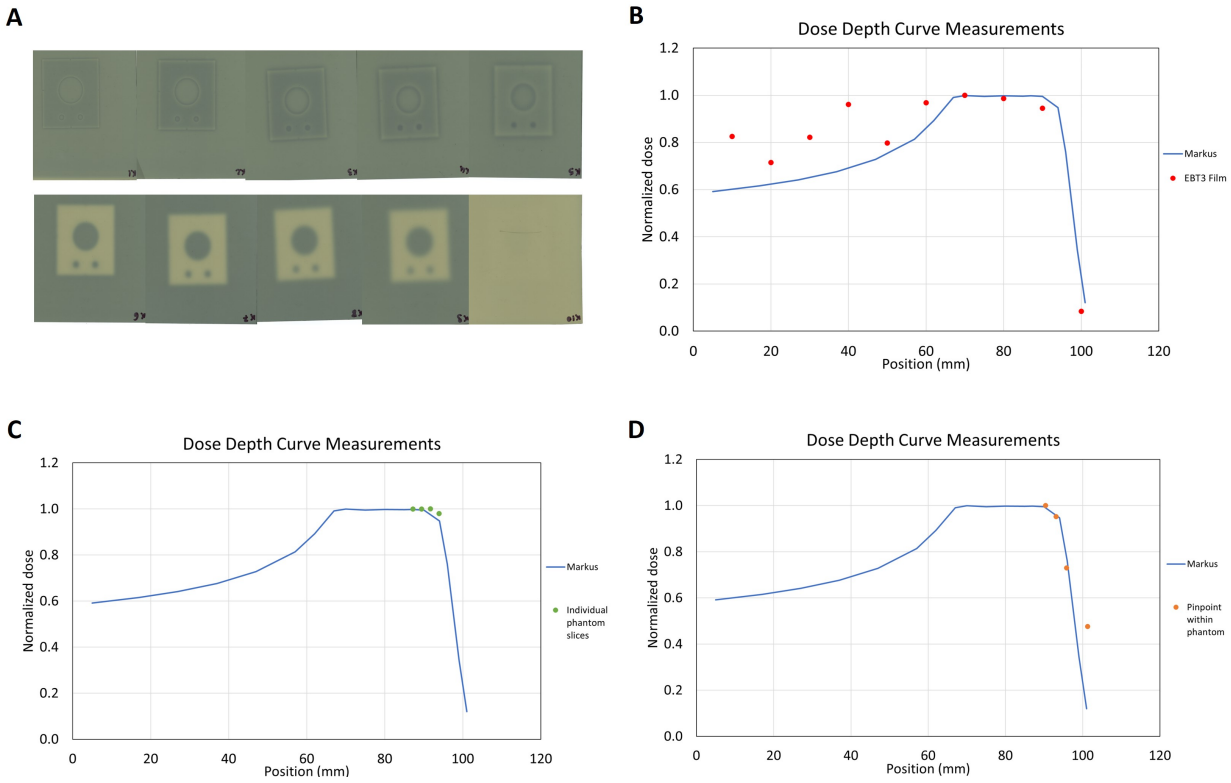

Figure 3.4: Dose-depth measurements **(A)** The Bragg curve was measured with an advanced Markus chamber, depicted with the blue line. EBT3 film was used to measure the same Bragg curve, represented by the red dots. Everything is normalised to 1. **(B)** Individual slices of the phantom were measured with an advanced Markus chamber (green dots), using the same setup. **(C)** In orange are the measurements obtained with a pinpoint detector at different places within the phantom

4

Discussion

During pre-clinical research of proton therapy, it is important to validate the dosimetry for accurate and representable results. To ensure that research outcomes can eventually be implemented in clinical practices, it is equally as important to also take biological effects into account. The main objective of this thesis was, therefore, to dosimetrically and biologically commission a pre-clinical proton therapy research line. A 3D-printed phantom was designed and irradiated to check accurate positioning in the beamline. Simultaneously, spheroids of head-and-neck tumour cells were characterised as biological commissioning, with the eventual goal of putting those two together.

4.1. 2D and 3D Cell Characterisation

First, the dose response of a 2D monolayer of cells and 3D spheroids was analysed and defined. 3D spheroids were chosen as they should better mimic the biological behaviour of a tumour, with similar heterogeneities and cell-cell interactions that are not observed in a 2D monolayer of cells. However, the dose response of the spheroids to proton radiation has not yet been fully understood.

It was shown that using Matrigel as ECM is a viable and relatively easy method for forming spheroids. Throughout time, the spheroids stayed fairly round, making for easier quantifications. However, there was a bit of variation between the sizes of the spheroids, which could complicate some quantifications. However, other studies that used various methods observed such a variance in size as well [29, 35].

The spheroids grew a lot faster in the first week after the irradiation than in the last week. A possible explanation could be found in the place where they were incubated. During the first week, the plates with spheroids were incubated at HollandPTC. In this incubator, almost no other plates were placed, meaning that the incubator was not opened a lot. In the second week after the irradiations, the spheroids were incubated at the RID. This incubator was used a lot more often, leading to higher variations in temperature and CO_2 levels. The transport itself could also have had an effect on the growth of the spheroids, however, a study by Roohani et al. found no significant difference in tumour spheroid growth when transported to a different location [37]. Still, significant differences were observed in the growth of the spheroids after 13 days when irradiated with 6 or 8 Gy. Yet, spheroids irradiated with 4 Gy did not show a significant difference in growth. Microscopic images of the spheroids showed a lot of detached cells in the group irradiated with 8 Gy. As this was not observed as much in the control group, it seems that due to the irradiation cells of the outer layer were killed and got detached. However, it should be investigated if these detached cells are indeed dead, possibly by collecting them and performing a clonogenic survival.

In these experiments, spheroids were only followed for 13 days after they were irradiated. However, it could be possible that a growth delay of irradiated spheroids is only visible after a longer period of time. Raitanen et al. followed tumour spheroids from different cell lines for 30 days and only found major differences after around 15 days [29]. The FaDu spheroids should, therefore, be followed for a longer period of time before conclusions can be drawn about the growth delay of the irradiated spheroids.

The spheroids showed higher radioresistance than the cells grown as a monolayer when the viability of both was compared. The cells exhibited an exponential decrease in viability, similar to what is already known about the dose response of cells. It could be concluded from this that the viability based on the ATP production of the cells is a viable endpoint to use when the response of cells to proton irradiation is investigated. This is in line with the notion that mitochondria are one of the most important factors in the response of a cell to stress caused by ionising radiation [38]. Nonetheless, the same pattern is not observed for the viability of the spheroids. Spheroids irradiated with 4 Gy actually show a higher viability than the unirradiated ones. The spheroids that received 8 Gy did show a decrease, however, not by a lot. This is also observed in some cell lines studied by Raitanen et al., where only spheroids irradiated with 20 Gy showed a viability lower than 50%. It seems that the spheroids are able to repair lower doses of proton irradiation better than a monolayer of cells is able to. Only when doses of 6 Gy and higher are received it appears that the spheroids are not able to repair the damage any longer. A possible explanation could be found when looking at the oxygen heterogeneity of a spheroid. The concentration of oxygen is lower in the core of the spheroid and higher in the outer, proliferating layer. Additionally, it is known that when cells are exposed to ionising radiation, reactive oxygen species are formed, leading to oxidative stress and DNA damage [39]. As the concentration of oxygen is lower in the core cells, it could be the case that fewer ROS are formed there. Additionally, as the cell wants to balance the oxidative stress, ATP production increases to fuel antioxidant mechanisms, which could be a reason why the viability of the spheroids is higher in the 4 Gy irradiated cells, as the viability assay is based on the level of cellular ATP [39]. However, the formation of ROS and the amount of DSBs in the cells of different layers of the spheroids should be further investigated. Furthermore, another measure should be found that is able to represent the viability of spheroids, as this assay is only based on the ATP production of the cells.

Live and dead cells of the spheroids were stained in green and red, respectively, to assess the ratio of the necrotic and the live cells. A ring of green cells was observed in both the widefield and confocal images, with a ball of necrotic cells in the centre. This seems to be in line with the theoretical layers of the spheroids as shown in figure 1.3, albeit the necrotic core seemed to be rather large in the microscopic images. Nevertheless, it is not clear if the cells in this ring of green are the only live cells in the spheroids, or if the small ring is due to the fact that green light has a lower penetrating range than red light due to a lower wavelength and higher energy particles [40]. Hence, no conclusions can be taken from these images and the ratio of necrotic/live cells that were quantified from them. A possible solution is to embed the spheroids in paraffin and slice them before staining. Such histological experiments can give more insights into the distribution of live cells within the spheroid, and with that a deeper understanding of the viability of the spheroids after irradiations can be gained.

For a better understanding of the response of tumour spheroids to proton irradiation, further research must be conducted. Possible directions are the staining of the cells and spheroids with $\gamma H2AX$ antibodies. This will enable the visualisation of DNA breaks caused by ionising radiation and, therefore, study the damaging effects of proton radiation on the DNA more directly [41]. Additionally, as discussed above, the FaDu spheroids should be followed for a longer period of time after the irradiations and the viability assay should be performed at different time points, also further in time, enabling a comparison of the ATP response over time. Alternatively, a viability assay based on another endpoint could be used and compared. Lastly, spheroids should be sliced before staining to allow for better imaging of the whole spheroids.

4.2. Phantom Design

For the validation of the range of the proton beam, a phantom was designed and 3D-printed. The phantom used in this thesis was printed from PLA filaments only. However, for accurate range validation that mimics the different biological tissues present in a small animal, multiple materials should be used. The two materials that were investigated, PLA and ASA, both had a relative stopping power value in the soft tissue range. ASA showed a lower density and stopping power, and could thus be used for lower-density soft tissues, such as adipose, while PLA could be used for soft tissues with a slightly higher density. When using one of these materials with a lower infill, very low densities and stopping powers could be reached, as accidentally shown with the wrongly printed block 2.1. This could be

used for lung-like tissues. A downside to using lower infill regions within the phantom is the air pockets that arise. These can lead to unwanted scattering effects due to the many air-material interfaces. Alternatively, lightweight PLA (3DLabPrint) could be used. This material foams up to a certain extent when different temperatures are used during the printing, leading to lower densities without the many air gaps. As of now, the characteristics of more materials should be explored to find suitable candidates for tissues with higher densities, such as bone, as well. A possible material for bone-like tissues could be the copper fill material used for the 3D-printed collimator.

Apart from the material choice, the settings of the 3D printer have been found to make a difference as well [33]. However, in this thesis, only minor differences were found when changing some settings of the printer (table 3.1). Increasing the layer height from 0.1 mm to 0.2 resulted in slightly decreased HU values from 7 to -21. This observation is in line, albeit a smaller difference, with the research of Fonseca et al, in which they found an average difference of -48 HU when increasing the layer height from 0.06 to 0.10 mm. Using the blue PLA resulted in a higher HU value (45 HU) when compared to the yellow PLA (7 HU). Thus, different colours cannot be used interchangeably and should be investigated separately when used in the phantom. Furthermore, the layers must be printed perpendicular to the proton beam, to ensure as few air-material interfaces as possible along the path of the protons.

Additionally, for accurate range reduction in the phantom, the amount of material in front of the tumour should be equal to that of the tissues in terms of water equivalency. In this thesis, the fictive tumour was placed in the head-and-neck region. However, only a small amount of soft tissue is located in front of this tumour. Therefore, for a more inclusive validation of the range reduction, the tumour should be placed somewhere else within the mouse. That way, more tissues with different densities and stopping powers are in front of the tumour.

4.3. Phantom Irradiations

The overarching goal of this thesis was to dosimetrically and biologically validate the proton therapy research line with the use of a phantom. Dosimetric verification was reached using EBT3 radiochromic film placed within the 3D-printed phantom. The first three films represented the start, middle, and end of the tumour, followed by two additional films somewhat further in the phantom and a last film placed directly outside of the phantom. A certain number of RW3 slabs were positioned in front of the phantom to adjust the range of the Bragg peak. When the tumour in the phantom was placed at the end of the Bragg peak, the dose decreased gradually, not giving a uniform dose inside of the tumour. Apparently, more energy is deposited than expected in the first half of the phantom than based on the range reduction calculations. This is better represented in figure 3.3E, where it is evident that the second and third points are not in line with the rest of the points and not in line with the measured Bragg peak. The effect of the shape of the phantom is apparent in the line profiles as well. These profiles start quite flat, however, halfway through the phantom some curvature is shown in the profiles. This is best visible in the line profile of the last film, just outside of the phantom. It is clear that this is due to the shape of the phantom, as in the x-direction the profile is higher on the right side. This is due to the fact that the protons need to travel a longer path through the head than through the neck, which is located on the right side. In the y-direction, a dip is observed in the last line profile. This is explained by the fact that the neck is rounded from left to right, causing the phantom to be at its thickest in the middle. Therefore, protons needed to travel through less material on the lateral sides of the head and neck, leading to higher doses on both lateral sides.

After the addition of the compensator, flatter line profiles were observed all throughout the phantom. Thus, it can be concluded that the compensator performed as desired in terms of a uniform profile in the x- and y-direction. The shape of the average doses of all films resembles the end of the Bragg peak, where the tumour receives a uniform dose and the dose decreases rapidly afterwards. However, when placed in the measured Bragg peak, a small shift was observed. This could be due to miscalculations with the WET of PLA. The determination of the WET of PLA appeared to be more difficult than previously thought, as the water equivalency varied with the thickness of the 3D-printed object [12].

When the phantom was fully placed in the plateau of the SOBP, the films showed almost identical

profiles, as expected. However, the fourth film suddenly displayed a higher dose than the rest of the films. It could be possible that this effect is caused by the LET dependence of the film [42]. However, if this is the case, the effect should be even higher in the last film. Yet, it is not visibly observed in that film. Therefore, it is more likely that the higher dose in the fourth film is by the error of using film dosimetry. As the average doses are normalized to the highest dose, this fourth point causes the other points to be pushed down, leading to the misalignment in the measured Bragg peak. This could be validated using a Monte Carlo simulation program, such as TOPAS, to simulate the beamline with this phantom.

Even though in all experiments a dose of around 2 Gy was given, the absolute dose values obtained from the quantification of the film showed a large variation, with doses from 2 to 5 Gy in the first film. As this was way above the systematic error determined for the film quantifications, it seems that using radiochromic film is not the best method when verifying the dosimetry. The same high variation was observed in the dose depth measurements. A possible solution could be to use the pinpoint detector within the phantom instead, as this seemed to give much neater results. However, the film is useful when investigating the shape of the beam and collimator. A combination of film and the pinpoint detector could thus be beneficial.

Quite a lot of dose was given to the surrounding material. This was due to the fact that the tumour was a sphere of only 5 mm in diameter, while the collimator had a diameter of 12 mm. However, when using a smaller collimator, other, poorly understood effects, come into play, due to the extremely small field [43]. It was, therefore, chosen to use a slightly bigger collimator than actually desired for this thesis. However, when following up on this project and before actual mice are irradiated, research towards the possible use of a smaller collimator, while obtaining a similar uniformity and dose distribution, must be conducted.

Dose depth measurements with EBT3 film showed that the 3D-printed collimator did not work properly at the entrance of the Bragg peak. The higher-energy protons at the entrance were not completely stopped by the collimator. This probably also led to interactions around the edges of the collimator, as even higher doses were observed there. This effect was not visible in the measurements made with the advanced Markus chamber, probably because the Markus chamber measures only a very small volume at the centre (0.02 cm^3) and is equipped with a small protection lid that also stops some protons [44]. Even though the experiments were not carried out at the entrance of the Bragg peak, a thicker collimator should be designed to overcome these difficulties.

5

Conclusion

The main objective of this thesis was to design a method with which the dosimetry of pre-clinical proton therapy research can be commissioned. As proton therapy is a combination of physics and biology, it is important to commission such a research line dosimetrically, but also biologically, by looking at the response of the tumour cells. To that end, a 3D-printed phantom was designed using materials with comparable stopping power values to that of biological tissues. However, currently, only one material was used for the experiments. For a more extensive validation of the range reduction, multiple materials with stopping power values comparable to various tissues of the small animal should be studied and used. Furthermore, placing the fictive tumour at a different position with more varying tissues in front can help to prove that the range estimation is actually accurate, as it is not only the range of one tissue that is tested.

Experiments with the 3D-printed phantom showed a clear and positive effect of the compensator. Even though the results globally showed a correct placement of the phantom relative to the Bragg curve, film dosimetry proved to be difficult when it comes to the quantifications. The use of a pinpoint detector could be a solution, as shown by the depth dose curve measurements. Moreover, a bigger and thicker 3D-printed collimator should be printed to ensure that all protons are stopped.

Furthermore, the dose response of FaDu cells and spheroids to proton therapy was characterised. The growth delay of the spheroids and the viability of both the cells and the spheroids were used as biological endpoints. Significant differences in the growth of the spheroids when irradiated with 6 or 8 Gy were found, however, not when irradiated with lower doses. For a more complete picture, spheroids should be followed for a longer period of time. The viability of the cells corresponded well with earlier findings. However, it was found that the radiobiological response of 2D was not reflected in 3D, as it seems that the FaDu spheroids showed a higher radioresistance than the cells. The cause of the behaviour of the spheroids to the different doses of proton therapy should be further investigated.

After all these considerations have been taken into account, dosimetric and biological commissioning using the 3D-printed phantom with the tumour spheroids can be implemented to validate pre-clinical proton therapy research.

References

[1] H. Ritchie, F. Spooner, and M. Roser. “Causes of death”. In: *Our World in Data* (2018). URL: https://ourworldindata.org/causes-of-death.

[2] Dejene Tolossa Debela et al. “New approaches and procedures for cancer treatment: Current perspectives”. In: *SAGE Open Medicine* 9 (Jan. 2021), p. 205031212110343. ISSN: 2050-3121. DOI: 10.1177/20503121211034366.

[3] Yinghao Lv et al. “FLASH radiotherapy: A promising new method for radiotherapy (Review)”. In: *Oncology Letters* 24 (6 Oct. 2022), p. 419. ISSN: 1792-1074. DOI: 10.3892/ol.2022.13539.

[4] K B Gordon, D I Smyk, and I A Gulidov. “Proton Therapy in Head and Neck Cancer Treatment: State of the Problem and Development Prospects (Review).” In: *Sovremennye tekhnologii v meditsine* 13 (4 2021), pp. 70–80. ISSN: 2309-995X. DOI: 10.17691/stm2021.13.4.08.

[5] Wayne D Newhauser and Rui Zhang. “The physics of proton therapy”. In: *Physics in Medicine and Biology* 60 (8 Apr. 2015), R155–R209. ISSN: 0031-9155. DOI: 10.1088/0031-9155/60/8/R155.

[6] Chang Hyeuk Kim et al. “Ridge filter design for a particle therapy line”. In: *Journal of the Korean Physical Society* 64 (9 May 2014), pp. 1308–1313. ISSN: 0374-4884. DOI: 10.3938/jkps.64.1308.

[7] Arpit Chhabra, Katja Langen, and Minesh P. Mehta. “An overview of modern proton therapy”. In: *Chinese Clinical Oncology* 5 (4 Aug. 2016), pp. 48–48. ISSN: 23043865. DOI: 10.21037/cco.2016.05.06.

[8] Eike Rietzel and Christoph Bert. “Respiratory motion management in particle therapy”. In: *Medical Physics* 37 (2 Jan. 2010), pp. 449–460. ISSN: 00942405. DOI: 10.1118/1.3250856.

[9] J.K. van Abbema et al. “High accuracy proton relative stopping power measurement”. In: *Nuclear Instruments and Methods in Physics Research Section B: Beam Interactions with Materials and Atoms* 436 (Dec. 2018), pp. 99–106. ISSN: 0168583X. DOI: 10.1016/j.nimb.2018.09.015.

[10] P van der Tol and P Jin. “CT ED-HU calibration and validation”. In: (2018).

[11] Bhagat Chand et al. “Effect of CT number to relative electron density curves acquired at different tube voltage and current on radiotherapy dose calculation”. In: *Journal of Physics: Conference Series* 2267 (1 May 2022), p. 012140. ISSN: 1742-6588. DOI: 10.1088/1742-6596/2267/1/012140.

[12] Rui Zhang and Wayne D Newhauser. “Calculation of water equivalent thickness of materials of arbitrary density, elemental composition and thickness in proton beam irradiation”. In: *Physics in Medicine and Biology* 54 (6 Mar. 2009), pp. 1383–1395. ISSN: 0031-9155. DOI: 10.1088/0031-9155/54/6/001.

[13] Carlos Eduardo de Almeida and Camila Salata. *Absolute, Reference, and Relative Dosimetry in Radiotherapy*. Ed. by Thomas J. FitzGerald and Maryann Bishop-Jodoin. IntechOpen, Oct. 2022. DOI: 10.5772/intechopen.101806.

[14] R. Speller et al. *Biomedical Sensors of Ionizing Radiation*. Ed. by D.P Jones. Momentum Press, LLC, 2010, pp. 129–238.

[15] Gerarda van de Kamp et al. “DNA Double Strand Break Repair Pathways in Response to Different Types of Ionizing Radiation”. In: *Frontiers in Genetics* 12 (Sept. 2021), p. 1771. ISSN: 16648021. DOI: 10.3389/FGENE.2021.738230/BIBTEX.

[16] Wonhee Hur and Seung Yoon. “Molecular Pathogenesis of Radiation-Induced Cell Toxicity in Stem Cells”. In: *International Journal of Molecular Sciences* 18 (12 Dec. 2017), p. 2749. ISSN: 1422-0067. DOI: 10.3390/ijms18122749.

[17] Maria P. Souli et al. “Clustered DNA Damage Patterns after Proton Therapy Beam Irradiation Using Plasmid DNA”. In: *International Journal of Molecular Sciences* 23 (24 Dec. 2022), p. 15606. ISSN: 1422-0067. DOI: 10.3390/ijms232415606.

[18] Anna R. Poetsch. “The genomics of oxidative DNA damage, repair, and resulting mutagenesis”. In: *Computational and Structural Biotechnology Journal* 18 (2020), pp. 207–219. ISSN: 20010370. DOI: 10.1016/j.csbj.2019.12.013.

[19] Gloria E. Villalpando-Rodriguez and Spencer B. Gibson. “Reactive Oxygen Species (ROS) Regulates Different Types of Cell Death by Acting as a Rheostat”. In: *Oxidative Medicine and Cellular Longevity* 2021 (Aug. 2021), pp. 1–17. ISSN: 1942-0994. DOI: 10.1155/2021/9912436.

[20] Susan Elmore. “Apoptosis: A Review of Programmed Cell Death”. In: *Toxicologic Pathology* 35 (4 June 2007), pp. 495–516. ISSN: 0192-6233. DOI: 10.1080/01926230701320337.

[21] A.R. Mitteer. “Proton beam radiation induces DNA damage and cell apoptosis in glioma stem cells through reactive oxygen species”. In: *Scientific Reports* 5 (1 Sept. 2015), p. 13961. ISSN: 2045-2322. DOI: 10.1038/srep13961.

[22] Clemens Grassberger et al. “Variations in Linear Energy Transfer Within Clinical Proton Therapy Fields and the Potential for Biological Treatment Planning”. In: *International Journal of Radiation Oncology*Biology*Physics* 80 (5 Aug. 2011), pp. 1559–1566. ISSN: 03603016. DOI: 10.1016/j.ijrobp.2010.10.027.

[23] Harald Paganetti. “Proton Relative Biological Effectiveness – Uncertainties and Opportunities”. In: *International Journal of Particle Therapy* 5 (1 Aug. 2018), pp. 2–14. ISSN: 2331-5180. DOI: 10.14338/IJPT-18-00011.1.

[24] Stephen J McMahon. “Proton RBE models: commonalities and differences”. In: *Physics in Medicine Biology* 66 (4 Feb. 2021), 04NT02. ISSN: 0031-9155. DOI: 10.1088/1361-6560/abda98.

[25] Armin Lühr et al. ““Radiobiology of Proton Therapy”: Results of an international expert workshop”. In: *Radiotherapy and Oncology* 128 (1 July 2018), pp. 56–67. ISSN: 01678140. DOI: 10.1016/j.radonc.2018.05.018.

[26] B. Jones. “Clinical radiobiology of proton therapy: modeling of RBE”. In: *Acta Oncologica* 56 (11 Nov. 2017), pp. 1374–1378. ISSN: 0284-186X. DOI: 10.1080/0284186X.2017.1343496.

[27] Harald Paganetti et al. “Relative biological effectiveness (RBE) values for proton beam therapy”. In: *International Journal of Radiation Oncology*Biology*Physics* 53 (2 June 2002), pp. 407–421. ISSN: 03603016. DOI: 10.1016/S0360-3016(02)02754-2.

[28] Raja Vadivelu et al. “Microfluidic Technology for the Generation of Cell Spheroids and Their Applications”. In: *Micromachines* 8 (4 Mar. 2017), p. 94. ISSN: 2072-666X. DOI: 10.3390/mi8040094.

[29] Julia Raitanen et al. “Comparison of Radiation Response between 2D and 3D Cell Culture Models of Different Human Cancer Cell Lines”. In: *Cells* 12 (3 Jan. 2023), p. 360. ISSN: 2073-4409. DOI: 10.3390/cells12030360.

[30] Louis-Bastien Weiswald, Dominique Bellet, and Virginie Dangles-Marie. “Spherical Cancer Models in Tumor Biology”. In: *Neoplasia* 17 (1 Jan. 2015), pp. 1–15. ISSN: 14765586. DOI: 10.1016/j.neo.2014.12.004.

[31] Sarah C. Brüningk et al. “3D tumour spheroids for the prediction of the effects of radiation and hyperthermia treatments”. In: *Scientific Reports* 10 (1 Feb. 2020), p. 1653. ISSN: 2045-2322. DOI: 10.1038/s41598-020-58569-4.

[32] Sreenivasulu Gunti et al. “Organoid and Spheroid Tumor Models: Techniques and Applications”. In: *Cancers* 13 (4 Feb. 2021), p. 874. ISSN: 2072-6694. DOI: 10.3390/cancers13040874.

[33] Gabriel P. Fonseca et al. “Dual-energy CT evaluation of 3D printed materials for radiotherapy applications”. In: *Physics in Medicine and Biology* 68 (3 Feb. 2023). ISSN: 13616560. DOI: 10.1088/1361-6560/acaf4a.

[34] et al. Alssabbagh. “Evaluation of nine 3D printing materials as tissue equivalent materials in terms of mass attenuation coefficient and mass density”. In: *International Journal of ADVANCED AND APPLIED SCIENCES* 4 (9 Sept. 2017), pp. 168–173. ISSN: 2313626X. DOI: 10.21833/ijaas.2017.09.024. URL: http://www.science-gate.com/IJAAS/V4I9/Alssabbagh.html.

[35] Suran Kim et al. “Tissue extracellular matrix hydrogels as alternatives to Matrigel for culturing gastrointestinal organoids”. In: *Nature Communications* 13 (1 Mar. 2022), p. 1692. ISSN: 2041-1723. DOI: 10.1038/s41467-022-29279-4.

[36] Srinivasan K and James Jabaseelan Samuel E. “Studies on the tissue and water equivalence of some 3D printing materials and dosimeters”. In: *Radiation Physics and Chemistry* 198 (Sept. 2022), p. 110259. ISSN: 0969806X. DOI: 10.1016/j.radphyschem.2022.110259.

[37] Siyer Roohani et al. “Photon and Proton irradiation in Patient-derived, Three-Dimensional Soft Tissue Sarcoma Models”. In: *BMC Cancer* 23 (1 June 2023), p. 577. ISSN: 1471-2407. DOI: 10.1186/s12885-023-11013-y.

[38] Dietrich Averbeck and Claire Rodriguez-Lafrasse. “Role of Mitochondria in Radiation Responses: Epigenetic, Metabolic, and Signaling Impacts”. In: *International Journal of Molecular Sciences* 22 (20 Oct. 2021), p. 11047. ISSN: 1422-0067. DOI: 10.3390/ijms222011047.

[39] Mina Răileanu et al. “Proton irradiation induced reactive oxygen species promote morphological and functional changes in HepG2 cells”. In: *Journal of Structural Biology* 214 (4 Dec. 2022), p. 107919. ISSN: 10478477. DOI: 10.1016/j.jsb.2022.107919.

[40] T.J. Bruno and P.D.N. Svoronos. *CRC Handbook of Fundamental Spectroscopic Correlation Charts*. CRC Press, 2005. ISBN: 9781420037685. URL: https://books.google.nl/books?id=FgjHjhCh5wsC.

[41] L-J Mah, A El-Osta, and T C Karagiannis. “γH2AX: a sensitive molecular marker of DNA damage and repair”. In: *Leukemia* 24 (4 Apr. 2010), pp. 679–686. ISSN: 0887-6924. DOI: 10.1038/leu.2010.6.

[42] Sarah E Anderson et al. “A linear relationship for the LET-dependence of Gafchromic EBT3 film in spot-scanning proton therapy”. In: *Physics in Medicine Biology* 64 (5 Mar. 2019), p. 055015. ISSN: 1361-6560. DOI: 10.1088/1361-6560/ab0114.

[43] Monika Clausen et al. “Small field proton irradiation for in vivo studies: Potential and limitations when adapting clinical infrastructure”. In: *Zeitschrift für Medizinische Physik* (Nov. 2022). ISSN: 09393889. DOI: 10.1016/j.zemedi.2022.10.002.

[44] Uwe Titt et al. “Design and validation of a synchrotron proton beam line for FLASH radiotherapy preclinical research experiments”. In: *Medical Physics* 49 (1 Jan. 2022), pp. 497–509. ISSN: 00942405. DOI: 10.1002/mp.15370.

[45] M. Togno et al. “Ultra-high dose rate dosimetry for pre-clinical experiments with mm-small proton fields”. In: *Physica Medica* 104 (Dec. 2022), pp. 101–111. ISSN: 11201797. DOI: 10.1016/j.ejmp.2022.10.019.

[46] Manuel Rodriguez et al. “Commissioning of a novel microCT/RT system for small animal conformal radiotherapy”. In: *Physics in Medicine and Biology* 54 (12 2009), pp. 3727–3740. ISSN: 00319155. DOI: 10.1088/0031-9155/54/12/008. URL: https://www.researchgate.net/publication/26249550_Commissioning_of_a_novel_microCTRT_system_for_small_animal_conformal_radiotherapy.

[47] Katia Parodi et al. “Towards a novel small animal proton irradiation platform: the SIRMIO project”. In: *Acta Oncologica* 58 (10 Oct. 2019), pp. 1470–1475. ISSN: 1651226X. DOI: 10.1080/0284186X.2019.1630752.

[48] M. Jermoumi et al. “Comprehensive quality assurance phantom for the small animal radiation research platform (SARRP)”. In: *Physica medica : PM : an international journal devoted to the applications of physics to medicine and biology : official journal of the Italian Association of Biomedical Physics (AIFB)* 31 (5 July 2015), pp. 529–535. ISSN: 1724-191X. DOI: 10.1016/J.EJMP.2015.04.010. URL: https://pubmed.ncbi.nlm.nih.gov/25964129/.

[49] Chris D. Johnstone et al. “Multi-institutional MicroCT image comparison of image-guided small animal irradiators”. In: *Physics in medicine and biology* 62 (14 June 2017), pp. 5760–5776. ISSN: 1361-6560. DOI: 10.1088/1361-6560/AA76B4. URL: https://pubmed.ncbi.nlm.nih.gov/28574405/.

[50] BIPM. *Bureau International des Poids et Mesures*. URL: https://www.bipm.org/en/.

[51] Eric S. Diffenderfer et al. “Design, Implementation, and in Vivo Validation of a Novel Proton FLASH Radiation Therapy System”. In: *International Journal of Radiation Oncology*Biology*Physics* 106 (2 Feb. 2020), pp. 440–448. ISSN: 0360-3016. DOI: 10.1016/J.IJROBP.2019.10.049.

[52] GafChromic. *Gafchromic EBT films*. URL: http://gafchromic.com/gafchromic-film/radiotherapy-films/EBT/index.asp.

[53] Michele M. Kim et al. “Design and commissioning of an image-guided small animal radiation platform and quality assurance protocol for integrated proton and x-ray radiobiology research”. In: *Physics in medicine and biology* 64 (13 July 2019), p. 135013. ISSN: 13616560. DOI: 10.1088/1361-6560/AB20D9. URL: /pmc/articles/PMC8690893/%20/pmc/articles/PMC8690893/?report=abstract%20https://www.ncbi.nlm.nih.gov/pmc/articles/PMC8690893/.

[54] Bijan Arjomandy et al. “EBT2 film as a depth-dose measurement tool for radiotherapy beams over a wide range of energies and modalities”. In: *Medical Physics* 39 (2 Jan. 2012), pp. 912–921. ISSN: 00942405. DOI: 10.1118/1.3678989.

[55] Michael D. Jensen et al. “Implementation and commissioning of an integrated micro-CT/RT system with computerized independent jaw collimation”. In: *Medical Physics* 40 (8 Aug. 2013), p. 081706. ISSN: 2473-4209. DOI: 10.1118/1.4812422. URL: https://onlinelibrary.wiley.com/doi/full/10.1118/1.4812422%20https://aapm.onlinelibrary.wiley.com/doi/10.1118/1.4812422.

[56] S. Reinhardt et al. “Comparison of Gafchromic EBT2 and EBT3 films for clinical photon and proton beams”. In: *Medical Physics* 39 (8 Aug. 2012), pp. 5257–5262. ISSN: 00942405. DOI: 10.1118/1.4737890.

[57] Yi Fang Wang et al. “Dosimetric verification and commissioning for a small animal image-guided irradiator”. In: *Physics in Medicine and Biology* 63 (14 July 2018). ISSN: 13616560. DOI: 10.1088/1361-6560/AACDCD.

[58] Daphnée Villoing et al. “Technical note: Proton beam dosimetry at ultra-high dose rates (FLASH): Evaluation of GAFchromic™ (EBT3, EBT-XD) and OrthoChromic (OC-1) film performances”. In: *Medical Physics* 49 (4 Apr. 2022), pp. 2732–2745. ISSN: 00942405. DOI: 10.1002/mp.15526.

[59] Ming Yang et al. “Adaptation and dosimetric commissioning of a synchrotron-based proton beamline for FLASH experiments”. In: *Physics in medicine and biology* 67 (16 Aug. 2022). ISSN: 1361-6560. DOI: 10.1088/1361-6560/AC8269. URL: https://pubmed.ncbi.nlm.nih.gov/35853442/.

[60] PTW The Dosimetry Company. *PTW Bragg peak chamber*.

[61] N. Patrik Brodin, Chandan Guha, and Wolfgang A. Tomé. “Proposal for a Simple and Efficient Monthly Quality Management Program Assessing the Consistency of Robotic Image-Guided Small Animal Radiation Systems”. In: *Health physics* 109 (3 Suppl 3 2015), S190–S199. ISSN: 1538-5159. DOI: 10.1097/HP.0000000000000323. URL: https://pubmed.ncbi.nlm.nih.gov/26425981/.

[62] S. Gerlach et al. “Beam characterization and feasibility study for a small animal irradiation platform at clinical proton therapy facilities”. In: *Physics in medicine and biology* 65 (24 Dec. 2020). ISSN: 1361-6560. DOI: 10.1088/1361-6560/ABC832. URL: https://pubmed.ncbi.nlm.nih.gov/33157544/.

[63] Jeppe Brage Christensen et al. “Al2O3:C optically stimulated luminescence dosimeters (OSLDs) for ultra-high dose rate proton dosimetry”. In: *Physics in Medicine and Biology* 66 (8 Apr. 2021). ISSN: 13616560. DOI: 10.1088/1361-6560/ABE554.

[64] Patrik Gonçalves Jorge et al. “Design and validation of a dosimetric comparison scheme tailored for ultra-high dose-rate electron beams to support multicenter FLASH preclinical studies”. In: *Radiotherapy and Oncology* 175 (Oct. 2022), pp. 203–209. ISSN: 18790887. DOI: 10.1016/j.radonc.2022.08.023.

[65] John R. Zullo et al. “LiF TLD-100 as a Dosimeter in High Energy Proton Beam Therapy-Can It Yield Accurate Results?” In: *Medical Dosimetry* 35 (1 Mar. 2010), pp. 63–66. ISSN: 09583947. DOI: 10.1016/j.meddos.2009.03.001.

[66] Pankaj Pathak Praveen Kumar, Mishra Manisha Singh, and Pankaj Kumar Mishra. “Analytical Study of Flatness and Symmetry of Electron Beam with 2D Array Detectors”. In: *Journal of Cancer Science Therapy* 7 (10 2015). DOI: 10.4172/1948-5956.1000366.

[67] IBA Dosimetry. *IBA Zebra*. URL: https://www.iba-dosimetry.com/product/zebra.

[68] Elke Beyreuther et al. “Feasibility of proton FLASH effect tested by zebrafish embryo irradiation”. In: *Radiotherapy and Oncology* 139 (Oct. 2019), pp. 46–50. ISSN: 18790887. DOI: 10.1016/j.radonc.2019.06.024.

[69] Houda Kacem et al. “Comparing radiolytic production of H2O2 and development of Zebrafish embryos after ultra high dose rate exposure with electron and transmission proton beams”. In: *Radiotherapy and Oncology* 175 (Oct. 2022), pp. 197–202. ISSN: 0167-8140. DOI: 10.1016/J.RADONC.2022.07.011.

[70] Arthur Bongrand et al. “A Monte Carlo Determination of Dose and Range Uncertainties for Preclinical Studies with a Proton Beam”. In: *Cancers* 13 (8 Apr. 2021). ISSN: 2072-6694. DOI: 10.3390/CANCERS13081889. URL: https://pubmed.ncbi.nlm.nih.gov/33920758/.

[71] E. Tryggestad et al. “WE-D-330A-08: The Small-Animal Radiation Research Platform (SARRP): Commissioning a 225 KVp “small-Field” X-Ray Source for Monte Carlo-Based Treatment Planning”. In: *Medical Physics* 33 (6Part20 June 2006), pp. 2241–2241. ISSN: 2473-4209. DOI: 10.1118/1.2241749. URL: https://onlinelibrary.wiley.com/doi/full/10.1118/1.2241749%20https://onlinelibrary.wiley.com/doi/abs/10.1118/1.2241749%20https://aapm.onlinelibrary.wiley.com/doi/10.1118/1.2241749.

[72] L Vanderwaeren et al. “Clinical Progress in Proton Radiotherapy: Biological Unknowns”. In: *Cancers* 13 (604 2021).

[73] N Peters and et al. “Experimental assessment of inter-centre variation in stopping-power and range prediction in particle therapy”. In: *Radiotherapy and Oncology* 163 (2021), pp. 7–13.

[74] W Semmler, M Schwaiger, and M Kachelriess. *Molecular Imaging I*. Springer, 2008. ISBN: 978354072717-=0.

[75] MILabs. *MILabs Preclinical Imaging Systems*. URL: https://www.milabs.com/preclinical-imaging-systems/.

[76] CIRS. “Tissue-equivalent materials elemental composition data sheet: CIRS Project 1744-00”. In: (2020).

[77] W Schneider, T Bortfield, and W Schlegel. “Correlation between CT numbers and tissue parameters needed for Monte Carlo simulations”. In: *Phys. Med. Biol.* 45 (2000), pp. 459–478.

[78] QRM. *Micro-CT HA Phantom. For the calibration of CT values*. URL: https://www.qrm.de/en/products/micro-ct-ha-phantom/.

A

Supplementary Figures

Theoretical diameter (μm)	Measured diameter (pixels)
600	1088
623	1148
627	1156
600	1105
571	1040
627	1156

Table A.1: Glass beads of different known sizes were imaged and measured to obtain a pixel-to-micrometre conversion. They were imaged with the inverted light microscope at RID. A conversion of 1.834 pixels per μm was used

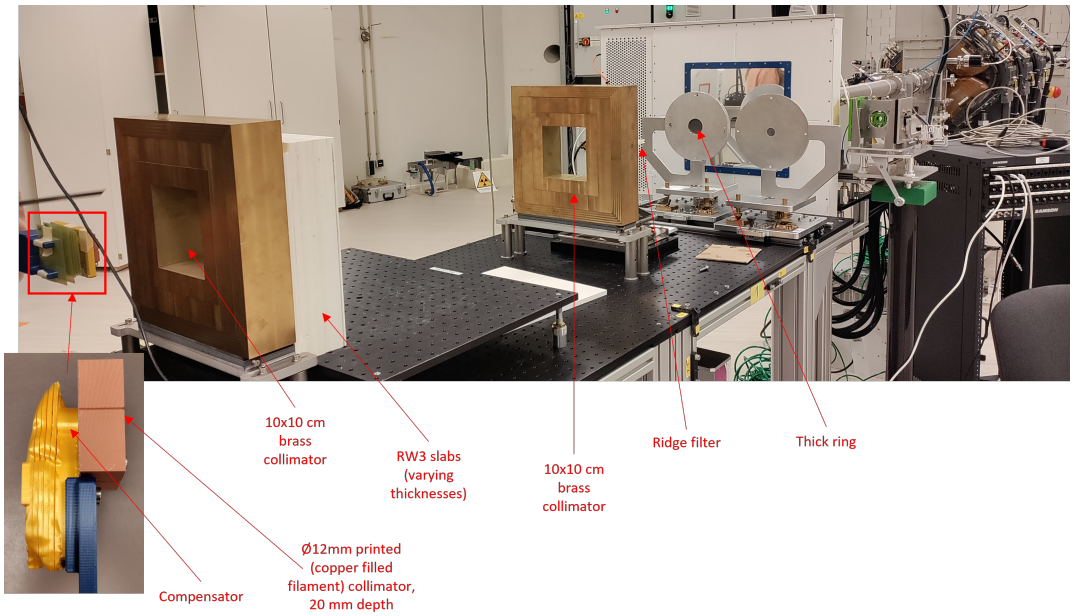

Figure A.1: A photo of the beamline setup at HollandPTC used for the phantom irradiations

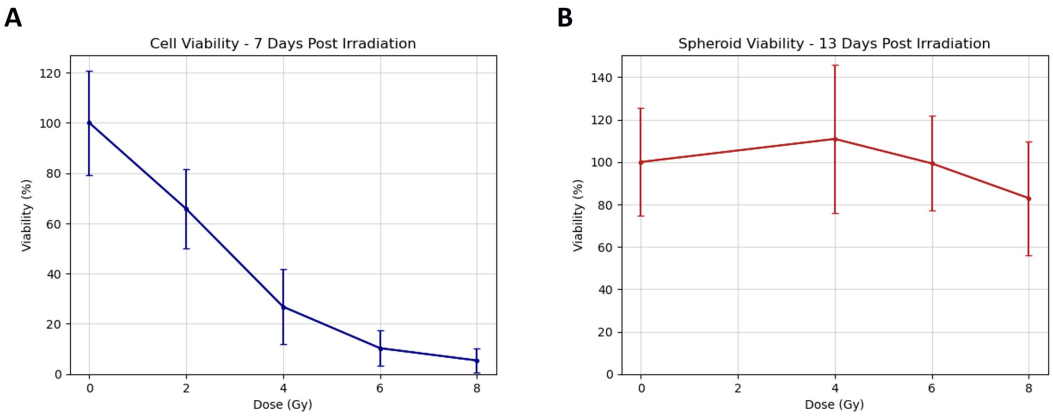

Figure A.2: Viability with standard error of the measurements **(A)** Viability of the cells, normalized to the control group (n=3, 6 measurements per experiment). The standard error is that of the pre-normalized measurements. **(B)** Viability of the spheroids, normalized to the control group (n=3, 6 measurements per experiment). The standard error is that of the pre-normalized measurements

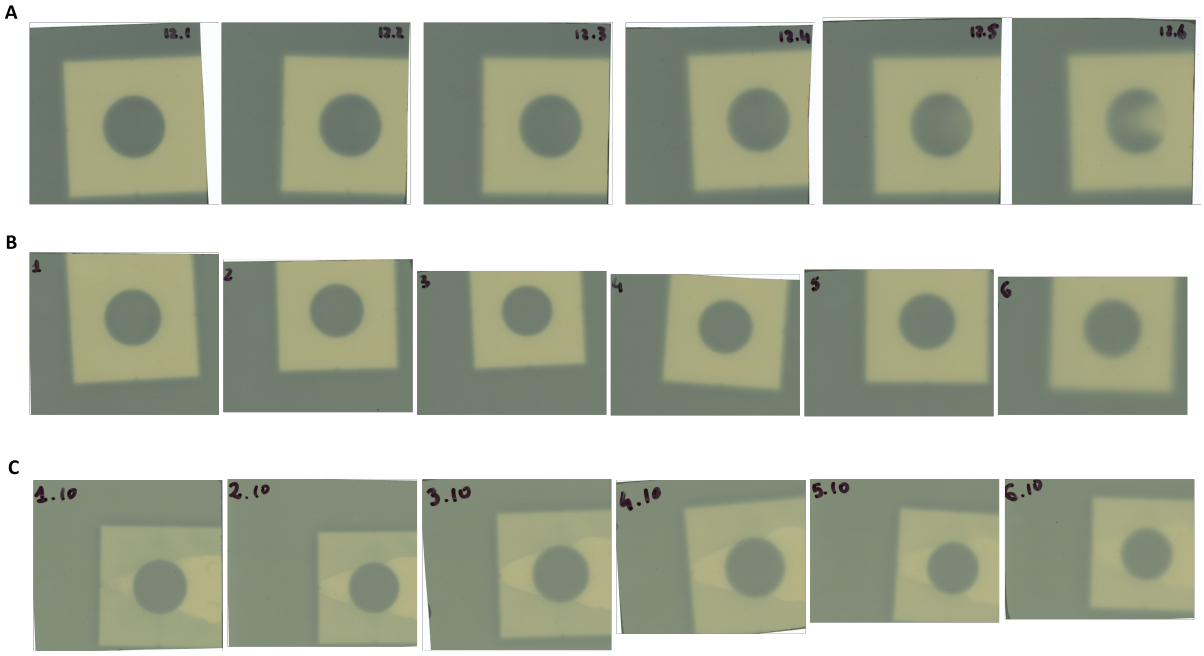

Figure A.3: Scanned radiochromic film of three experiments. **(A)** No compensator, 81 mm RW3. **(B)** Compensator, 72 mm RW3. **(C)** Compensator, 58 mm RW3. It can be seen, since the phantom is further back in the SOBP, that the collimator is again not able to stop all protons

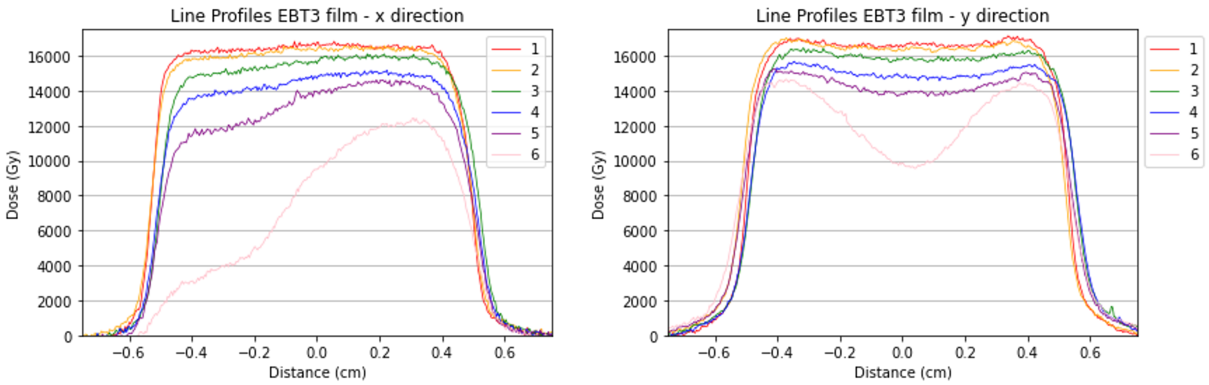

Figure A.4: Line profile plots from the grey values. No compensator, 81 mm of RW3. Same film as fig. 3.3C, but before calibration is applied

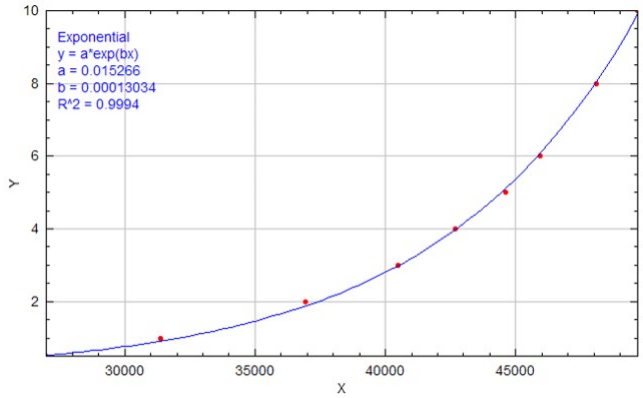

Figure A.5: Greyvalue-to-dose calibration used for the analysis of the irradiated EBT3 film

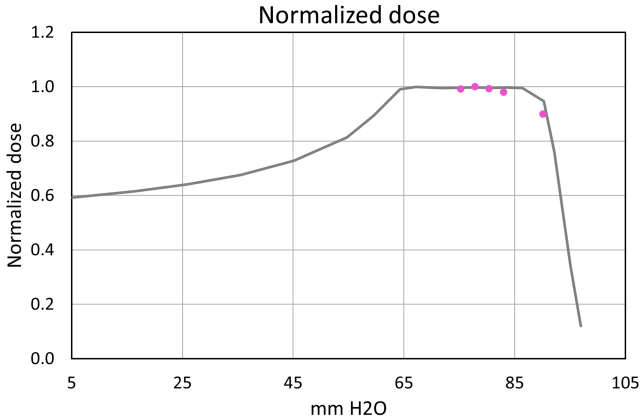

Figure A.6: The Bragg curve with the reanalysed normalised dose points obtained from the films irradiated with a compensator in the middle of the SOBP. From the same data as figure 3.3K, however, this analysis could not be reproduced a second time. The normalised dose points do align better with the Bragg curve, within the total systematic error. Maximum variation of 1% in the phantom and an intra-tumour variation of 0%

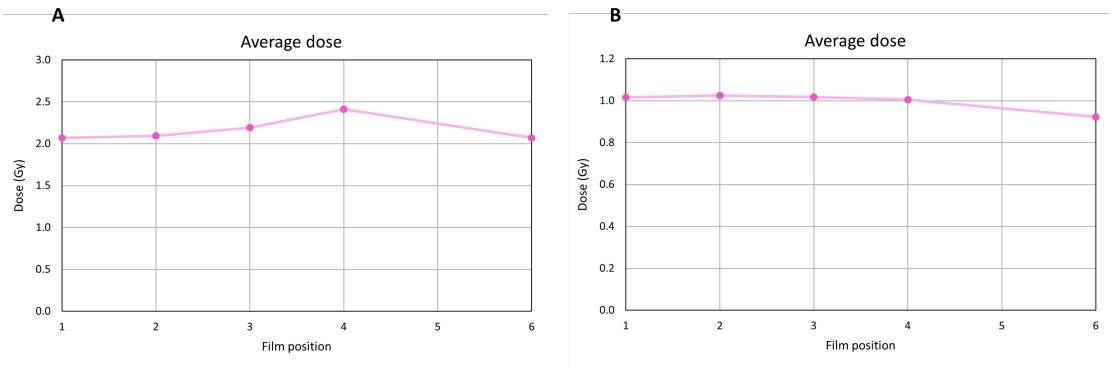

Figure A.7: Comparison of the reanalysis of the film irradiated with a compensator and 58 mm RW3. **(A)** First analysis, also figure 3.3J. **(B)** Reanalysis of the same film on a different computer. Note that the absolute dose values differ quite a bit

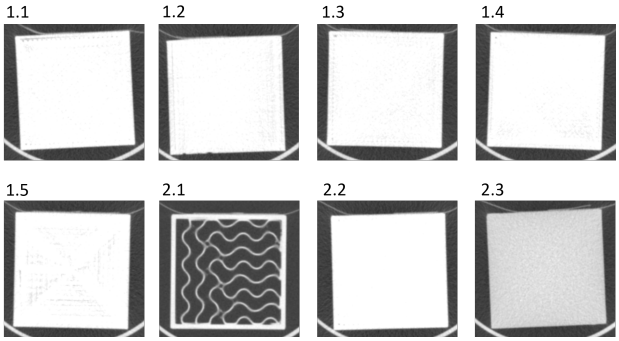

Figure A.8: Post-reconstructed CT scans of the blocks. A 3D median and 3D Gaussian filter were applied. The centre slice of the CT scan is depicted. Numbers correspond to the different printing settings (table 2.1)

B

Literature Recommendations on Dosimetric and Biological Commissioning

This literature review was written around January 2023 in preparation for this thesis. In this review, different approaches for dosimetric and biological commissioning are discussed in the context of a pre-clinical proton therapy research line. Phantoms are used for the commissioning of the micro-CT, with which image quality measures are determined, as well as for the characterisation of the proton beam. Radiochromic film is the simplest technique for relative dosimetric validation, ionization chambers are the best for absolute dosimetry. There is not a lot of research done on biological commissioning, however, promising approaches are being investigated. One phantom that can be used for the commissioning of the micro-CT, physical characterisation and dosimetry and biological dosimetry for simple and accurate commissioning of a proton therapy research line should be further investigated, as well as methods for treatment planning.

B.1. Introduction

Nowadays, most patients with cancer are being treated with radiotherapy. There are different types of radiotherapy, of which photon therapy is by far the most used in the clinic. Nevertheless, for some applications, proton therapy is becoming more popular due to its many advantages over photon therapy, the most prominent one being the decreased amount of dose deposited in the healthy tissue surrounding the tumour when compared to photon therapy. An important part of proton therapy is precise dose delivery. This is achieved using treatment planning, of which there are two types: forward and inverse planning. In forward planning, beams are placed according to a CT scan after which the dose is calculated. In inverse planning, the tumour and critical organs are defined on a CT scan, and target doses are given, after which an optimisation program is run to find the best treatment plan. This is used more often, as it can handle complex situations.

As the biology of proton therapy and more specific techniques such as FLASH is very complex, pre-clinical research is being carried out. During this research, precise dose delivery is important, as well as dose verification. Quality assurance programs already exist in the clinic, but an equivalent for pre-clinical systems is likewise needed [45] [46].

Additionally, biological responses of the irradiated tissues are not fully uncovered but play a major role in how the radiation is received. It is, therefore, important to study *in vivo* small animals to elucidate these unknowns [47]. However, as small animals are being used, the to-be-irradiated structures are very small as well, thus submillimetre information is needed for the correct range of the proton beam. This can be regulated using dosimetric validation. Physical dosimetric validation is needed to ensure a high accuracy from the proton beam and, therefore, correct dose delivery and biological dosimetric

validation is needed to include the biological responses into the system. Furthermore, to avoid variation between and within studies, some kind of quality assurance is needed.

Therefore, the goal of this review is to find out what is already written about the dosimetric and biological commissioning of a small-animal proton therapy research line. This search will be divided into different sections according to the different parts of a commissioning pipeline. First is the commissioning of a micro-CT setup, followed by dosimetric validation and characterisation of a proton beam and the biological dosimetric validation, concluded by treatment planning and dose calculation techniques.

B.2. Literature Review

B.2.1. Commissioning of a micro-CT setup

For the commissioning of a microCT setup, the image quality is determined. As pre-clinical treatment plans for proton irradiations are made based on the microCT image, on the stopping power calculations as well as on the geometry, and especially for small animals even a millimetre difference can mean irradiating a different tissue, the image quality of the microCT images is of high importance. Different research groups have used various methods to assess this quality, which will be discussed in this section.

In 2015, Jermoumi and his colleagues [48] developed a quality assurance (QA) phantom that can, among other things, be used for the assessment of the image quality of a micro-CT scanner. To this end, reconstructed images of a solid water slab were used, with which they established image accuracy, defined as the distance per pixel of the image object, uniformity, and noise. The uniformity of the image is measured by taking the difference between the intensity of a pixel at the centre of the slab and the intensity of a pixel at the outer limits. The noise was quantified as the standard deviation of the intensity of the pixels. Additionally, they also performed a quality assurance of the accuracy of the CT numbers. For this, they used images of a slab that contains inserts of tissue-equivalent material from the lungs and bones, and they calculated the CT number as follows:

$$CTnumber = \frac{I - I_{water}}{I_{water}} * 1000, \tag{B.1}$$

where I is the intensity of the pixel. The values that they found were compared to a baseline, which they acquired by collecting data over a month time. They concluded that performing the QA in this manner is a reasonable way to assess the image quality. They also state, however, that it could be improved by including some more tests, for example, a high contrast resolution test.

In 2017, the team of Johnstone [49] created a quality assurance software that can be used to assess the image quality of the microCT. For this, they use a phantom which is called the Shelley phantom. This phantom has different plates, each of which can be used to quantitatively assess a different metric for image quality. An image of the six different plates can be found in figure B.1. After imaging, the CT numbers are first converted to Hounsfield Units by setting the CT numbers of water and air to -1000 HU and 0 HU, respectively, and linearly inter- and extrapolating the other tissue-equivalent materials that are enclosed in the phantom, as can be seen in figure B.1f. This is immediately the assessment of the first image quality metric, namely the CT number evaluation. Next is the CT number linearity, necessary for the accuracy of the dose calculations. This is determined using different concentrations of iodine solutions in the upper left plate in figure B.1, which are plotted against their Hounsfield unit. From this, the linearity can be determined by calculating the fit of the line. The same plate is also used to calculate the signal-to-noise ratio (SNR), using the following formula:

$$SNR = \frac{\mu}{\sigma}. \tag{B.2}$$

Another measure they determined with their QA program is image uniformity. For this, they plotted a line profile through the upper middle plate in image B.1. An ideal line profile should show a CT number of 0 HU throughout the whole centre of the plate, with at both sides a sharp increase in HU for the sides, and afterwards a sharp decrease to around -1000 HU for where the plate has ended. This is of course disrupted by noise, which can be quantified by taking the standard deviation of a region of interest in the middle of the plate.

The geometric accuracy plate, shown in figure B.1c, consists of five tungsten-carbide beads. From this, the geometric accuracy can be calculated as the in-plane voxel size:

$$in-planevoxelsize = \frac{d_{known}}{d_{measured}}, \tag{B.3}$$

where d_{known} is the known physical distance between neighbouring beads and $d_{measured}$ is the measured distance between the centre of the neighbouring beads, both measured in voxels. The last image quality metric they used for their QA program, is spatial resolution. They used two plates for this: the coil plate, consisting of four coils of aluminium and plastic with different thicknesses, and the slanted edge plate, consisting of a slanted edge from a tilted air-polycarbonate plastic boundary. The spatial resolution is then determined by the modulation transfer function (MTF) as follows:

$$MTF(f) = \frac{\pi\sqrt{2}}{4}\frac{M(f)}{M_0}, \tag{B.4}$$

where M(f) is the average standard deviation from each coil, and M_0 is the absolute difference of the HU for aluminium and the HU for plastic, divided by two. For the slanted edge plate, it is slightly more difficult to get to the MTF, as first an edge-spread function (ESF) is determined by a line profile, which is differentiated to get the line spread function (LSF), which in turn can be converted to the MTF by calculating its Fourier transform. The image quality measures above are all important for the image quality QA, as they affect the geometric accuracy, which in turn affects the dosimetric accuracy, either directly (CT number linearity), or indirectly due to the correct identification of the tissues in the small animals.

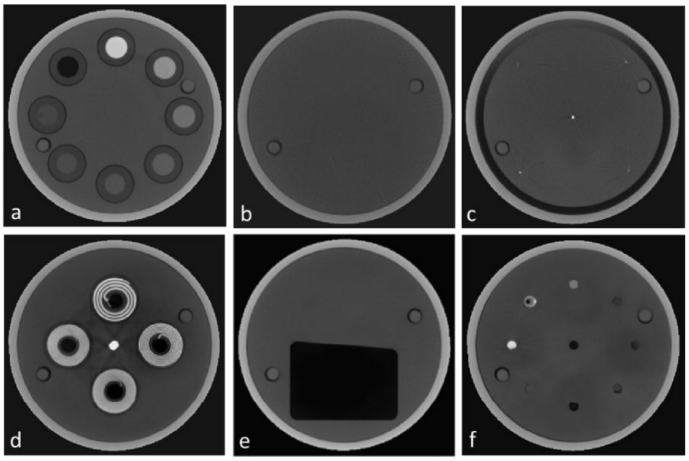

Figure B.1: This image shows the six plates from the Shelley phantom. The plates are used for assessing different image quality measures: (a) CT number linearity, (b) uniformity and noise, (c) geometric accuracy, (d) spatial resolution (coil), (e) spatial resolution (slanted edge), and (f) CT number evaluation. The images are obtained with a micro-CT scanner [49]

B.2.2. Dosimetric Validation

During irradiation, a very low uncertainty of the delivered dose is desired to assure that the correct dose is deposited in the tissue. Therefore, the dosimetric measurements need to represent the correct value, also when compared to the same measurements of different institutions, which maybe have a slightly different protocol or use a different device. Absolute dosimetry is therefore used to ensure that the measurements are highly accurate when compared to its definition. Absolute dosimetry measurements are first executed by so-called Primary Standards Dosimetry Laboratories (PSDL). These laboratories are equipped with the highest quality instruments to be able to measure the quantities in an absolute way. The BIPM [50], an organization where the international system of measurement is located, compares all the different National PSDLs to each other to establish consistency between all absolute dose measurements. There are more locations in one country that use this high-quality equipment, the so-called Secondary Standards Dosimetry Laboratories (SSDL), and they are calibrated by the nation's PSDL.

The rest of the laboratories are calibrated by the SSDLs to maintain a network of comparable results [13]. Absolute dose measurements can be performed with a Farmer chamber or a Markus chamber, the use of which will be discussed later. When dosimetric measurements are performed without calibration by absolute dose measurements, it is called relative dosimetry. This is sometimes advantageous to use, as it is independent of the setup used for the absolute dosimetry.

It is of importance for pre-clinical research to have consistent dosimetry to ensure the right dose delivery in the system, therefore, dosimetric validation is needed [46][51]. Different methods, using absolute dosimetry, as well as relative dosimetry, for dosimetric validation are discussed in this section.

A lot of researchers that are performing experiments in which they do some kind of dosimetric validation, use radiochromic film. Radiochromic film is often yellow or green, but when it is exposed to radiation, the dye polymerizes and gives a shade of blue to the film [14]. Using its optical density, the dose that the film was exposed to can be determined. The most used radiochromic film is from GafChromic dosimetry films [52]: Gafchromic EBT film. Advantages of using radiochromic film are that it can be used without special film processing steps, and it can just be cut in any size or shape that is needed for the experiment. This makes it easy to handle and work with in different experimental settings. It is also only sensitive to ionizing radiation, and can thus be used in normal settings, without the need for it to be dark in the room. Additionally, it has a weak energy and dose rate dependence, and the optical density of the dye in the film does not change over time, all of which are useful characteristics when using the film for dosimetric validation research. However, the group of Diffenderfer and Kim [53] state that in the high LET regions of the Bragg peak, the Gafchromic film proves to be unreliable, which is difficult when employing the radiochromic film for dosimetric validation. Arjomandy et al. [54] studied this effect and stated that it is due to quenching effects.

EBT2 Gafchromic film is used for dosimetric validation studies amongst others by Rodriguez et al. [46], although they used a photon beam instead of a proton beam, by Jensen et al. [55], and by Jermoumi et al. [48]. Around the publishing of that paper, Gafchromic developed an improved radiochromic film, the EBT3 series. Reinhardt and her team [56] made a comparison between the EBT2 and the EBT3 film and they concluded that there is no significant difference in the performance between the two, except for the eradication of the dependence on the orientation of the film in the EBT3 film. From around that year, most researchers used the EBT3 Gafchromic film for the dosimetry of proton beams. Wang et al. [57] showed that the EBT3 Gafchromic film can be used for accurate small-field dosimetry, while Togno et al. [45] used the film successfully for dosimetry in the ultra-high dose rate dosimetry regions. Kim et al. used film to measure beam profiles and determined some beam characteristics from these measurements.

Gafchromic also developed another EBT film: the EBT-XD, developed for working in a higher dose range. Villoing et al. [58] compared the dose rate dependency of EBT3 and EBT-XD film, and they found that both types of film give an overestimation of doses beyond 10 Gy and should therefore be used with caution in those regions. Yang et al. [59] used EBT-XD film for dosimetric commissioning by validating the absolute dose measurements done by a Markus chamber. They found that the results from the EBT-XD measurements were well-matched to the Markus chamber measurements, with a mean difference of 0.32%. Similar experiments with EBT-XD film were conducted by Titt et al. [44].

Different types of ion chambers can be used for absolute dose measurements, among which the Markus chamber and the Farmer chamber [60]. Rodriguez et al. [46] used an ionization chamber to measure the dose rate as a function of the depth. Their experiments were. however, performed with a photon beam. Jensen et al. [55] used a Farmer chamber to measure the beam output, just like Brodin et al. [61], while Kim et al. [53] used a Markus chamber for absolute dosimetry, similar to Diffenderfer et al. [51]. In 2020, Gerlach et al. [62] used a Bragg peak chamber [60], which is a parallel-plate ionization chamber that is able to measure exactly where the Bragg peak is located, to determine the integral depth dose (IDD). The determination of the IDD measures not only the point dose, but includes the halo surrounding it as well.

Yet another method is studied very recently by Togno et al. [45]. To verify the delivered dose, they

first performed a calibration of a plane-parallel ionization chamber. This calibration yielded a curve in terms of Monitor units per deposited dose (MU/Gy), where the plane-parallel ionization chamber is used as the primary monitor. The response of this ionization chamber was then compared to the measurements of a Faraday cup, the calibration curve of which was used to verify the Monitor Units per delivered proton (MU/p ratio). Additionally, they used a synthetic single-crystal microDiamond, which is a transmission chamber, for real-time dosimetry. First, This transmission chamber is calibrated using a Farmer chamber to get absolute dose measurements. Then, after each irradiation, this transmission chamber checks the delivered charge in terms of delivered Coulomb per proton (Coulomb/p). This is again compared to the measurements from the Faraday cup. They found that using the plane-parallel ionization chamber gives a robust calibration curve and that this method, therefore, proves to be reliable for the use of dosimetric measurements.

Apart from these ion chambers, there are also some alternative dosimeters used. Jermoumi et al. [48] performed dosimetric measurements with the nanoDot optically stimulated luminescent dosimeter (OSLD), just as Togno et al. [45]. Advantages of these detectors are described by Christensen et al. [63], from the same group as Togno. They state that OSLDs are able to perform dosimetric measurements with high precision while being dose-rate independent and suitable for small sizes. Another dosimeter is the thermoluminescent dosimeter (TLD), used by for example Jorge et al. [64]. In 2010, Zullo et al. [65] studied the accuracy of dosimetric measurements made by TLDs and they found that the results were in agreement with absolute dose measurements made by an ionization chamber.

B.2.3. Characterisation of a Proton Beam

Another aspect of the commissioning pipeline is the characterization of the proton beams. As unknown differences between proton bundles can lead to an inhomogeneously irradiated tumour, commissioning of this beam is essential to ensure a low uncertainty in the dose delivery during treatments [46]. Several studies include some kind of beam characterization in their commissioning research. In this section, a few methods found in the literature will be reviewed.

Often used beam characterizations include beam flatness, beam symmetry, width of the penumbra, full-width half-maximum (FWHM), and dose depth. Beam flatness is defined as the ratio of the highest and the lowest dose from the middle 80% of the area of the beam, whereas beam symmetry is defined as the ratio of the doses of two symmetric points at either side of the beam axis [66]. Penumbra refers to the region at the edge of the proton beam, where the dose falls off quickly. It is generally calculated by taking the distance between 20% and 80% of the maximum dose. The FWHM is the field size of the proton beam at 50% of the proton beam.

Rodriguez et al. [46] used Gafchromic EBT film to determine the beam flatness, beam symmetry, penumbra, and FWHM already in 2009. The Gafchromic EBT film was also used to analyze the dose rate as a function of depth. For this, they used a phantom of solid water, in which pieces of film were placed. With the data that they obtained from these provisions, the researchers found that these characteristics are suitable for use in dosimetric validation. These experiments were, however, performed for a photon beam. Similarly, Kim et al. [53] used EBT3 film to analyze the beam profiles for multiple energies, and Jensen et al. [55] used EBT2 film for determining beam characteristics.

Kim et al. [53] used a different method to obtain the depth curve of the beam. They used the IBA Zebra device [67], an ion chamber device that can measure the depth dose distribution. With this device, the percentage depth dose (PDD) was measured for different energies of the beam. This device is made for particle therapy rooms, thus the resolution is not high enough for the range in which small-animal are located. Kim and his colleagues resolved this by using paper index cards, of which they first determined the water equivalent thickness (WET) before measuring the depth dose with the detection chamber. They performed the same measurements of the PDD using the PTW Bragg peak chamber. This Bragg peak chamber is a plane-parallel chamber used to verify the exact position of the Bragg peak [60]. They found that it was still a challenge to analyze the dosimetric characteristics of a proton beam used for small animals, due to its size and relatively low beam energies. The ion chambers used are created for clinical dose measurements, therefore, because of the small sizes, partial volume av-

eraging occurs. To mitigate this problem, the authors suggest microchambers as a solution, as these are used for small x-ray fields because of their smaller measurement volumes. However, this should first be studied more for proton particles.

B.2.4. Biological Dosimetric Validation

Biological responses play an important role in the response of the tissue to proton irradiations [47]. Therefore, biological dosimetry, verification and validation in a well-characterized biological system, is a necessary step in the commissioning of a small-animal proton therapy research line. There are several research groups that have studied some kind of commissioning of a proton therapy line with biological samples, a couple of which will be discussed in this section.

In 2019, Parodi et al. [47] aimed to verify the range *in vivo*. One method they used to accomplish this, was the use of *in situ* positron emission tomography (PET) imaging. PET imaging is a technique that forms an image using gamma rays, which are emitted when a 511 keV photon pair collides. Not only is an in-beam PET scanner useful for biological image guidance, but it can also determine the range of a proton beam by measuring the β^+-activity induced by the radiation. They found that it is spatially challenging, but their tests showed encouraging results.

Beyreuther et al. [68] used zebrafish embryos as a model to study irradiations with a proton beam. They used a scintillation detector and EBT3 Gafchromic film to determine the dose homogeneity, and two ionization chambers, a beam monitor ionization chamber and a Bragg peak ionization chamber, to determine the dose delivery. Kacem et al. [69] also used zebrafish embryos, to study ultra-high dose rates of the proton beam. They determined the survival rate and anomalies induced by the radiation by looking at the body length and by using immunofluorescence and confocal microscopy. They state that using the zebrafish embryo as a model for radiobiological experiments has advantages such as it being a full *in vivo* model with a fast biological response and being easy to analyze.

Optically stimulated luminescence detectors (OSLDs) were already used for dosimetric validation, as seen in section 2.2, but Christensen et al. [63] used OSLDs in a setup for radiobiologic experiments. In this study, they used water-filled vials, as well as vials filled with biological samples, to show that the OSLD can provide dosimetry suitable for radiobiological experiments with a proton beam.

B.2.5. Treatment Planning and Dose Calculations

One of the final steps in small-animal proton therapy is treatment planning. For pre-clinical treatment planning, researchers use slightly different methods, which will be discussed in this section.

During this literature research, the most used method by far is Monte Carlo simulations. This statistics-based technique can construct a dose distribution of a certain treatment by sending a certain amount of points through a modelled beamline to a CT image of the subject. By scoring these points, dose distributions can be calculated. For example, Rodriguez et al. [46] used their work on the dosimetrics, pieces of which are described in the sections above, for a Monte Carlo simulation that is used for calculations for treatment planning. Jensen and his group [55] also used Monte Carlo simulations which they calibrated against the measurements they obtained with the ion chamber, described in section 2.2. Additionally, they validated their model by comparing the results of the simulation to the measurements they obtained with the EBT2 radiochromic film. They found an uncertainty of 3% or less for the Monte Carlo dose verification, which could be due to modelling errors, but it could also be due to errors in the measuring, as radiochromic film has its challenges for small animal dosimetry. Furthermore, Yang et al. [59] used Monte Carlo simulations to compare the depth dose to the measurements they made with a Markus chamber. They found dose differences within 2%, except at the top of the Bragg peak, where the variation was double. The authors state that this overestimation of the Monte Carlo simulation is not uncommon in regions where the dose gradient is very sharp.

Wang et al. [57] used Monte Carlo modelling not only for dose calculations but also to determine beam characteristics. They compared these simulations to measurements obtained with EBT3 film

and found that they were very similar, indicating that Monte Carlo modelling can be used for dosimetric commissioning of small animal proton therapy. Similarly, Monte Carlo simulations are used by Gerlach et al. [62], Bongrad et al. [70], and Tryggestad et al. [71].

B.3. Discussion

The aim of this literature review was to investigate what has been published about the dosimetric and biological commissioning of a small-animal proton therapy research line. In this section, the results of this search will be discussed in light of a practical method to perform dosimetric commissioning during pre-clinical research.

Commissioning a micro-CT scanner is challenging due to the submillimetre size that is needed for working with small animals. The most important parameter to commission the micro-CT on is the image quality. As treatment plans can be made using micro-CT images, even a millimetre difference can mean a different structure in the animal, which leads to a different range of the proton beam. It was found in the literature that mainly simple phantoms are used to establish different measures for image quality, such as CT number evaluation and linearity, uniformity and noise, and geometric and spatial accuracy. Determination of these measures worked fine using simple phantoms, there is no real need for more complex methods or phantoms. Of the myriad of phantoms, the Shelley phantom stood out because of its multiple plates which enable fast and easy micro-CT commissioning. However, most of the studies discussed in this literature review performed commissioning of the micro-CT in a photon research line, instead of for protons. Regardless, this is not a problem, as it is about the image quality of the micro-CT, in which the eventual radiotherapy beam does not yet play a role.

It is important to ensure that the correct dose is given at the proper position, dosimetric measurements are used to verify this. A lot of studies that perform some kind of dosimetric validation were found for this study, indicating that this is more widely seen as a necessary step. As seen in section 2.2, radiochromic film is the easiest to use for relative dosimetry due to its many advantages. However, it was also found that the radiochromic film showed inaccuracies, especially around the high-LET region of the Bragg peak. Therefore, different ionization chambers can be used, by some papers even viewed as the golden standard for dosimetric validation. Contrary to what radiochromic film is mostly used for, ionization chambers give absolute dosimetric results, which is sometimes desirable. Thus, for the best dosimetric verification, also at the high-LET region of the Bragg peak,

Commissioning of a proton beam is mainly done by defining beam-specific characteristics, like beam flatness, beam symmetry, the width of the penumbra, FWHM, and the dose depth. Papers included in this review used either Gafchromic EBT film or ionization chambers to determine these measures, which proved to work satisfactorily for this purpose. An advantage to using radiochromic film or an ionization chamber is that it can be done simultaneously with the dosimetric verification, as discussed in the paragraph above.

It seems like biological dosimetry in a proton research line is only just starting to arise, as quite recent papers that involve some kind of biological dosimetry in pre-clinical proton therapy studies appeared. This is positive, as biological validation is a crucial part of the commissioning of the research line, as biological responses play an important role in how the radiation is received by the tissue. It is therefore useful to implement biological modelling in treatment planning. Luckily, there are some very promising ideas explored in this review. One of the ideas discussed is the use of an *in vivo* PET scanner to enable *in vivo* range verification. This is would be beneficial as during the irradiation the range of the proton beam can be checked. However, the implementation of a whole PET scanner in the proton beamline is challenging due to the size and structure of the machines. Another idea that is discussed above is employing zebrafish embryos as a model. They are a widely used model in biological research as it is a complete *in vivo* model with a fast reproduction time. They are easy to analyze using any form of microscopy as the embryos are transparent and thus light can travel through them, and fluorescent markers are relatively easy to implement. One problem, however, is the size of the embryos. As they are even smaller than the already fairly small mice, the structures of the tissues

are even smaller, which makes it especially hard to verify the range of the proton beam. Even when immobilized, it is problematic to obtain submillimetre-accurate spatial information. On the other hand, they do not only have to be used for range verification but there can also be looked at the survival and morphogenic alterations of the embryos, as the studies discussed in section 2.4 did, which can give information about if the correct dose is given to the embryos. Furthermore, these methods can be used in combination with specific fluorescent markers to study some cellular responses to proton irradiation. Therefore, using zebrafish embryos as a model has a lot of potential and definitely needs to be explored further in this context. The last method of biological dosimetric validation that is discussed above, is the use of vials filled with biological samples in combination with an OSLD. This is valuable as the vial can be filled with human cells, maybe even in 3D cultures, to study the biological reaction of human biological samples. This is also a reasonably easy technique to implement, as these vials are small in size and methods to analyze cellular responses are already utilised.

One concept that arises from this review is to combine multiple elements, for example, a phantom with radiochromic film pieces inside and a vial in which a biological sample can be stored. This way, there is one phantom that can be employed for the commissioning of the micro-CT, for dosimetric verification and for biological validation. However, this needs to be further examined before this can be implemented in pre-clinical research.

There is not a lot published about treatment planning for pre-clinical proton therapy. This is probably due to the complexity of some proton therapy systems when compared to treatment planning for passive scattering photon therapy, for example. What is found about treatment planning for proton therapy mainly uses Monte Carlo simulations to compute a dose distribution. This technique proved to be quite accurate and is comparable to what is used in treatment planning for photon therapy. However, there is still a lot of research to be done and techniques to be explored in this area as this is a really relevant topic which can eventually be extended to treatment planning in the clinic.

B.4. Conclusion

Physical, dosimetric and biological commissioning of various parts of the small-animal proton therapy research line is essential to ensure the proper dose delivery and, hence, reliable, reproducible, and consistent outcomes. Over the last few years, more studies have been done concerning commissioning, using various methods explored in this literature review. For the commissioning of the micro-CT, image quality is the most important measure. Image quality can be established by determining different metrics that display the image quality with the use of phantoms. One phantom that really stood out is the Shelley phantom, which has six plates for various purposes. Physical characterisation of the proton beam is best done with a simple phantom that can be used to define simple parameters of the bundle. For dosimetric validation, a combination of radiochromic film for relative dosimetry and an ionization chamber for absolute dosimetry can be used. This combination ensures an as accurate as possible view of the delivered dose, given the error the radiochromic film gives around the high-LET region of the Bragg peak. There is still a lot more research needed for the validation of proton therapy in biological samples. Steps forward have been taken by, for example, using zebrafish embryos as a model or by integrating a PET scanner in the beamline, however, this needs a lot of work before it can fully be integrated into the research line for the biological validation. Research should be done towards one phantom that can be used for the commissioning of the micro-CT, physical characterisation and dosimetry and biological dosimetry for simple and accurate commissioning of a proton therapy research line.

C

Micro-CT Calibration

In 3D dose calculations for proton therapy, the spread-out Bragg peak (SOBP) needs to be located at the right place. For that, the predicted range of the protons through the tissues is needed. This can be determined by using the stopping power ratio. In this project, a CT calibration on a micro-CT scanner is successfully performed to relate the CT number, which depends on the photon energy, to the stopping-power ratio for protons, in order for this scanner to be used for preclinical proton therapy studies. Additionally, the acquisition and reconstruction of the micro-CT images are optimized.

C.1. Introduction

Radiation therapy is widely used as a treatment for cancer. In current clinical practice, photons are used for irradiation, however, instead of photons, protons are more and more used in some instances. This is due to their advantageous physical properties, which limit the dose deposited in healthy tissue surrounding the tumour while increasing the dose administered to the tumour [72]. In figure C.1 it can be seen that protons deposit most of their dose at the end of their range, dropping off quickly after. This so-called Bragg peak can be placed where it is needed by adjusting the energy of the protons. By combining multiple Bragg peaks, a spread-out Bragg peak (SOBP) is created, where the peak is able to enclose the whole tumour [72], ensuring a homogeneous dose to the tumour and none to little beyond.

To be able to place this spread-out Bragg peak in the right place, determination of the range of the protons is needed. This range can be predicted by the stopping power ratio (SPR) [73]. To calculate the stopping power ratio, different characteristics of the tissues the protons travel through are needed. These characteristics can be determined using a CT scanner. Using the CT number and a series of materials with known properties, a link can be made from the CT number to the stopping power ratio.

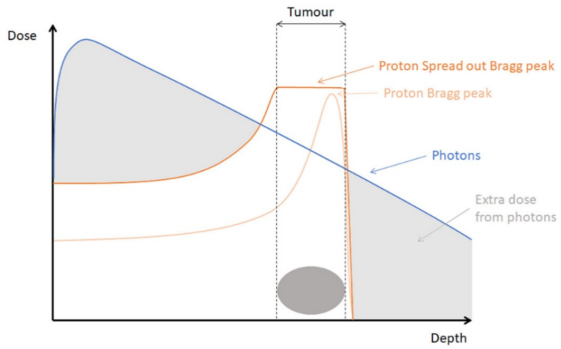

Figure C.1: In this figure the depth-dose distributions of photons and protons can be seen. Figure from Vanderwaeren et al. [72]

Name Insert	Density (g/cm^3)	H	C	N	O	Mg	P	Cl
lightgrayAir	0.00012	0	0	75.5	23.2	0	0	0
lightgray Lung Inhale	0.205	8.59	65.92	3.52	19.27	0	0	1.69
lightgray Lung Medium	0.31	7.91	54.78	2.47	25.71	8.14	0	0.95
Adipose	0.96	9.97	71.36	1.79	16.37	0	0	0.19
30% Gland + 70% Adipose	0.97	9.67	70.72	1.96	16.73	0	0	0.22
Water	1	11.19	0	0	88.81	0	0	0
70% Gland + 30% Adipose	1.011	9.52	69.8	1.9	17.26	0	0	0.18
Gland	1.048	9.41	69.13	1.84	17.66	0	0	0.14
Soft Tissue Gray	1.055	8.47	57.44	1.65	24.59	7.62	0	0.19
Spinal Cord	1.061	8.46	56.21	1.53	24.78	8.41	0.12	0.18
Kidney	1.068	8.52	62.95	1.97	20.63	4.45	0	0.16
Brain Tissue	1.069	8.16	53.6	1.53	26.49	9.98	0	0.19
Prostate	1.077	7.44	55.8	2.24	25.9	8.41	0	0.2
Spinal Disk	1.131	6.71	45.76	1.88	31.06	14.36	0	0.21
lightgray Trabecular Bone	1.197	7.46	54.84	1.3	25.28	2.12	0	0.11
lightgray 30% Cortical + 70% Trabecular	1.34	6.53	49.85	1.51	23.76	0	5.56	0.07
lightgray 70% Cortical + 30% Trabecular	1.617	4.88	36.92	1.17	29.13	1.21	8.19	0.04
lightgray Cortical Bone Core	1.91	3.3	25.37	0.91	35.28	3.36	8.82	0.03

Table C.1: A list of the material properties of the different CIRS inserts [76] and water and air. The elemental composition is in %

Details of how this is done can be found in the section **??**. Subsequently, when a treatment plan is being made, a CT scan of the tumour and its surroundings can be made. Using the defined relation, the stopping power ratio can be determined for each voxel separately, the predicted range can be computed, and the SOBP can be located correctly. This is the basis for a 3D dose calculation and is necessary before radiation treatment.

As described above, CT scans are needed, not only for the anatomy of the tumour and its surroundings but also to make a treatment plan by predicting the range of the protons. For this project, a micro-CT scanner will be used, as clinical CT scanners cannot achieve a spatial resolution high enough for small animals that are used in preclinical proton therapy studies [74].

This brings us to the goal of this project: optimize the acquisition and reconstruction of the micro-CT images and perform a CT calibration on the VECTor micro-CT scanner from MILabs [75] to relate the CT number, which depends on the photon energy, to the stopping power ratio for protons, in order for this scanner to be used for preclinical proton therapy studies.

C.2. Methods

C.2.1. CT Imaging

A phantom with human tissue-like inserts is normally used for clinical CT calibrations. For this project, such a phantom made by CIRS is used. For the CT calibration of a micro-CT scanner, only the inserts of this phantom are used, as the whole phantom is too big to fit into the scanner. These inserts have a density and elemental composition that is similar to certain tissues in the human body. An overview of the different inserts and their density and composition can be found in table C.1 [76]. Additionally, a tube filled with Milli-Q water is used to attain the CT information on water and air. Their densities and composition can also be found in table C.1.

Micro-CT scanning was performed using the VECTor micro-CT scanner from MILabs [75]. There were two slightly different setups used. The first setup used the default settings for rat CT imaging: a tube voltage of 55 kV, a tube current of 170 μA, 4m29 scanning time, 75 ms exposure time, and a 0.5 mm Al filter. A rat bed was used to lay the inserts on with a piece of tape ensuring the same placement for all inserts. For the second setup, only the tube voltage changed to 50 kV. This tube voltage is more commonly used for mice CT imaging, which is why this voltage was chosen for the second setup.

For both these setups all 18 inserts, also counting water and air, were imaged with ultra-focus, creating a FOV of 64 mm. After imaging the CT images were reconstructed using a voxel size of 72 μm over 278 slices with a Hann projection filter.

C.2.2. Post-Reconstruction

The reconstructed CT images were processed with first a 3D median filter ($\sigma_{x,y,z} = 2$ pixels) and after a 3D Gaussian filter ($\sigma_{x,y,z} = 2$ pixels). This was done to reduce the amount of noise while preserving the details for higher image quality. The filtering was performed in ImageJ. The image quality was quantitatively assessed using the contrast-to-noise ratio (CNR), which was calculated as follows [74]:

$$CNR = \frac{\mu_{insert} - \mu_{air}}{\sigma_{insert}}. \tag{C.1}$$

C.2.3. CT Calibration

The mean HU values and standard deviations were obtained by taking a circular region of interest in the middle three slices of the CT images of a particular insert and averaging these. This was done using the ImageJ software and a macro to automate the process and prevent human influence as much as possible. An initial calibration was performed by forcing the mean HU values of water and air to 0 and -1000, respectively, to comply with the definition of a CT number. All the other HU values are mapped accordingly in a linear fashion.

To be able to calculate the stopping power for each voxel tissue properties for that specific voxel are needed. Therefore, a relation between the CT number and the tissue properties can be used. In the paper by Schneider et al., they did exactly that [77], only for photons. However, in this paper, the method by Schneider et al. is adopted and implemented for protons as described below.

First, scanner-specific values are needed; k_1 and k_2. They are defined as $k_1 = \frac{\overline{K}^{sca}}{\overline{K}^{KN}}$ and $k_2 = \frac{\overline{K}^{ph}}{\overline{K}^{KN}}$, where K^{KN} is the Klein-Nishina coefficient, K^{sca} the scattering term, and K^{ph} the photoelectric absorption term. These terms represent the physical processes that determine the attenuation of the X-rays and are scanner-dependent. k_1 and k_2 can be determined by carrying out a least square fit of the measured CT numbers, i.e. minimizing the following expression:

$$\sum_{n=1}^{18} \left[\left(\frac{\overline{\mu}}{\overline{\mu}_{H_2O}} (k_1, k_2) \right)_n - \left(\frac{H(meas)}{1000} + 1 \right)_n \right]^2, \tag{C.2}$$

where

$$\frac{\overline{\mu}}{\overline{\mu}_{H_2O}} = \frac{\rho}{\rho_{H_2O}} \frac{\sum_{i=1}^{n} (w_i/A_i)(Z_i + Z_i^{2.86} k_1 + Z_i^{4.62} k_2)}{(w_H/A_H)(1 + k_1 + k_2) + (w_O/A_O)(8 + 8^{2.86} k_1 + 8^{4.62} k_2)}, \tag{C.3}$$

the attenuation of the material relative to that of water. The second part of the least square fit follows from the following equation, which converts the attenuation values to Hounsfield units:

$$H = \left(\frac{\overline{\mu}}{\overline{\mu}_{H_2O}} - 1 \right) * 1000. \tag{C.4}$$

Once these values are known, the HU values of 72 known tissues from Schneider et al. are calculated using equation C.3 and C.4, from which the calibration curve can be plotted. This curve should have three distinct regions: first the lung-like tissues with the steepest slope, next the soft tissues, which are located quite close together, and lastly the bone tissues, with a wide range of HU values, but a less steep slope than the lung-like tissues.

Using the calibration curve just created, the density and elemental composition can be determined by fabricating regions of Hounsfield units in which the measured CT numbers can be divided into and assigned a density and elemental composition using the following equations:

$$\rho = \frac{\rho_1 H_2 - \rho_2 H_1 + (\rho_2 - \rho_1)\, H}{H_2 - H_1} \tag{C.5}$$

$$w_i = \frac{\rho\,(H_2 - H)}{(\rho_1 H_2 - \rho_2 H_1) + (\rho_2 - \rho_1)\, H}\,(w_{1,i} - w_{2,i}) + w_{2,i}, \tag{C.6}$$

where $H_1 \leq H \leq H_2$. The width of the bins of the regions depends on the standard deviation of the measured HU values and all bins together arches over the whole range of the scanner.

These steps are repeated for both the setups used for the CT imaging.

C.2.4. Stopping Power Calculations

The stopping power is defined as the loss of energy from the protons per unit path length through a tissue. The relative stopping power is calculated using the Bethe-Bloch formula, which can be seen below [10]. As can be seen in equation C.7, it is expressed relative to water, which, therefore, has a stopping power of 1 by definition.

$$RSP = \frac{\rho N_g}{\rho^{water} N_g^{water}} \frac{ln\left[2m_e c^2 \beta^2 / I_m \left(1-\beta^2\right)\right] - \beta^2}{ln\left[2m_e c^2 \beta^2 / I_{water}\left(1-\beta^2\right)\right] - \beta^2} \tag{C.7}$$

In this formula, N_g is the number of electrons per unit volume of material, and it can be calculated by [10]:

$$N_g = N_A \sum \frac{w_i Z_i}{A_i}. \tag{C.8}$$

I_m is the mean excitation energy of the atoms, which is calculated using the following formula [10]:

$$lnI_m = \frac{\sum \frac{w_i Z_i}{A_i} lnI_i}{\sum \frac{w_i Z_i}{A_i}}, \tag{C.9}$$

where

$$I_i = \begin{cases} I \approx 19.0eV & Z = 1, \\ I \approx (11.2 + 11.7 * Z)\, eV & 2 \leq Z \leq 13, \\ I \approx (52.8 + 8.71 * Z)\, eV & Z > 13. \end{cases} \tag{C.10}$$

For this project, the stopping power is calculated for all 18 materials using the known densities and elemental composition. These values are then compared to the stopping power values calculated from the determined densities and elemental composition from the calibration. These calculations are performed for both setups.

C.2.5. Validation of the CT Calibration

To validate the calibration, the micro-CT HA phantom by QRM was used to validate the calibration. This phantom consists of five inserts of various calcium hydroxyapatite ($Ca_5(PO_4)_3(OH)$) concentrations: 0, 50, 200, 800, and 1200 mg HA/cm^3 with densities 1.13, 1.16, 1.26, 1.65, and 1.90 g/cm^3, respectively, to mimic different bone tissue in mice [78]. These inserts are embedded in epoxy resin ($C_{21}H_{25}ClO_5$). Using these numbers and structural formula, the elementary composition can be calculated via the different volume- and mass fractions.

This phantom was imaged in the same manner as the CIRS inserts, also using a rat bed and the exact same two setups. Subsequently, the calibration of the corresponding setup was used to calculate the stopping power of the different inserts of the HA phantom as described in section C.2.4.

Additionally, the root mean square error is calculated as follows:

(a) (b)

Figure C.2: Both images are the middle slice of the CT images of the trabecular bone. On the left side, the insert is scanned with 50 kV, and on the right side it is scanned with 55 kV.

Setup	Filters	Mean CNR
55 kV	-	3.189116
55 kV	Median + Gaussian	41.9595
50 kV	Median + Gaussian	36.4255

Table C.2: Quantification of the image quality. The CNR is calculated for all 18 materials and then averaged.

$$RMSE = \sqrt{\frac{\sum_{i=1}^{N} \left(RSP_{theoretical} - RSP_{calibration}\right)^2}{N}}. \tag{C.11}$$

C.3. Results

C.3.1. CT Imaging

Two slices from the CT images of one of the materials, the trabecular bone insert, are shown in figure C.2. The figure shows the images after the reconstruction- and post-reconstruction steps. The circle in the middle is the insert, and the half-circle underneath it is the rat bed.

The results of the quantification of the image quality are tabularized in table C.2. It can be seen that the contrast-to-noise ratio is a lot higher when using a Median and Gaussian filter after the reconstruction and that it does not decrease much when using a lower tube voltage.

C.3.2. CT Calibration

The measured HU values from the CT images of all 18 materials, the CIRS inserts plus water and air, were mapped linearly to ensure the HU value of water and air to be 0 and -1000, respectively. These forced HU values can be found in the supplementary data, section C.6. When plotted against the density of all 18 materials, as shown in figure C.3, a characteristic calibration curve can already be seen, with a different slope for the lung materials, soft tissues, and bones. There are no major differences to be seen between both setups.

Next, the calibration curve was created for 72 known tissues. The resulting curves for both setups are shown in figure C.4. Again, the different slopes of the lung materials, soft tissues, and bones can be observed in both calibration curves. Also, still, no major differences are seen between both setups.

C.3.3. Stopping Power Calculations

The calculated relative stopping power values are graphed in figure C.5. All stopping power values can also be found in the supplementary data, in section C.6. It can be seen that the calculated stopping power values lie close to the theoretical values. There are also small differences between the two setups: the stopping powers that are calculated from the calibration resulting from the scans made with 55 kV are a lot closer to the theoretical stopping power values of the materials than the ones calculated from the calibration resulting from the scans made with 50 kV.

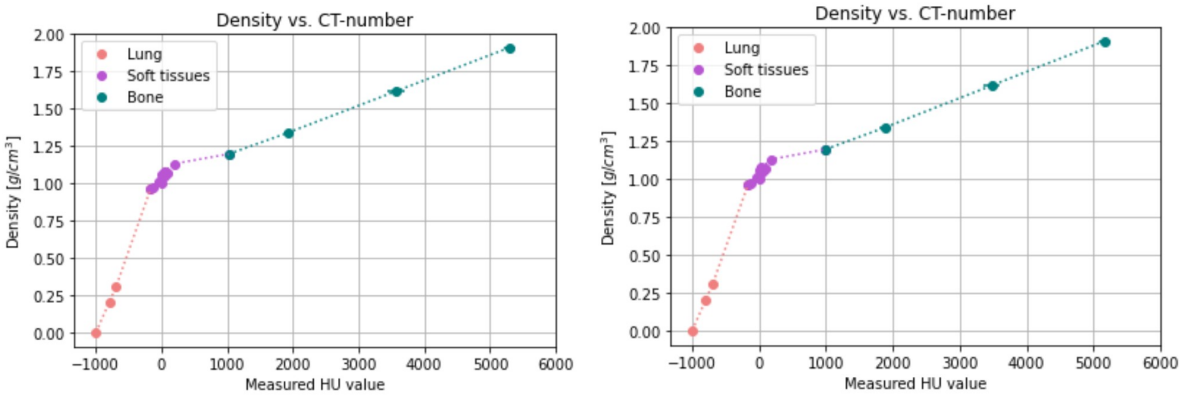

(a) **(b)**

Figure C.3: This figure shows the density vs. the CT-number (HU value) for (a) 50 kV and (b) 55 kV. Both figures have 18 data points; the CIRS inserts plus water and air.

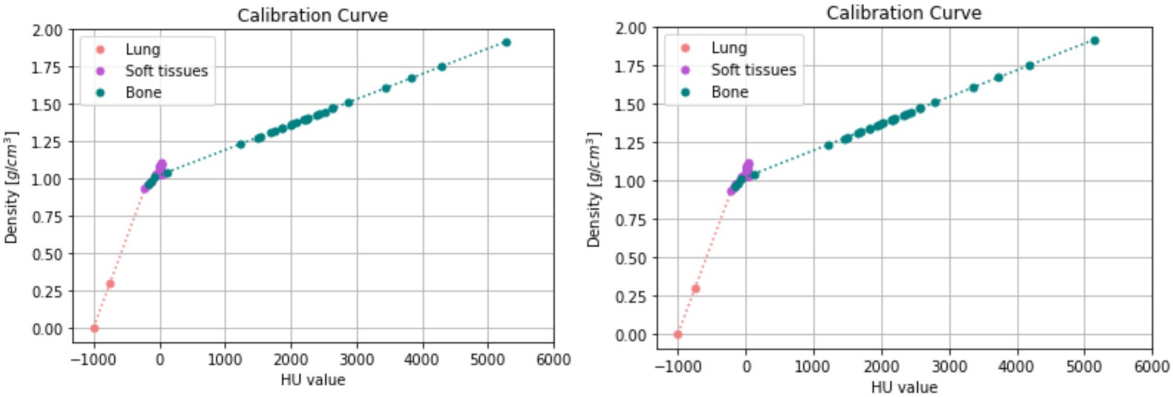

(a) **(b)**

Figure C.4: This figure shows the calibration curve for (a) 50 kV and for (b) 55 kV. The curves are based on 72 tissues.

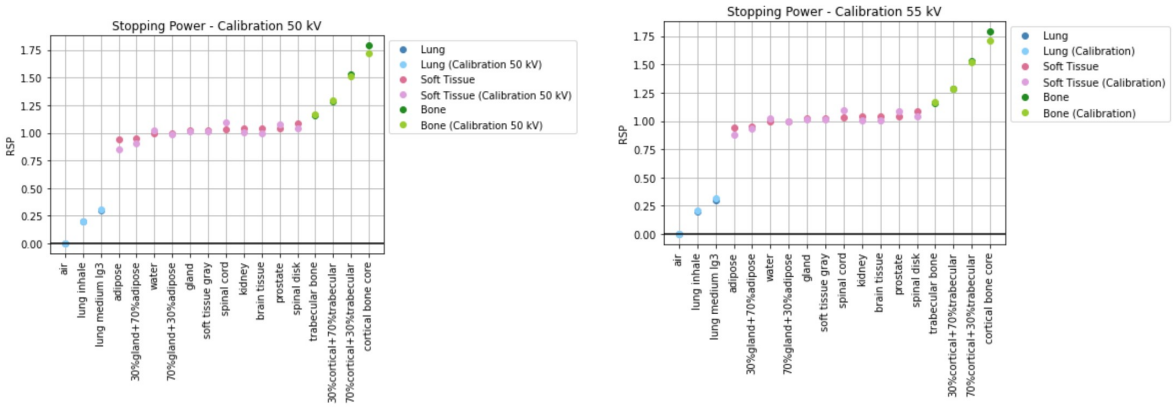

(a) (b)

Figure C.5: In this figure the relative stopping powers calculated using the calibration from the setup with (a) 50 kV and with (b) 55 kV are displayed. The darker-coloured dots are the theoretical stopping power values, and the lighter-coloured dots are the ones calculated via the calibration

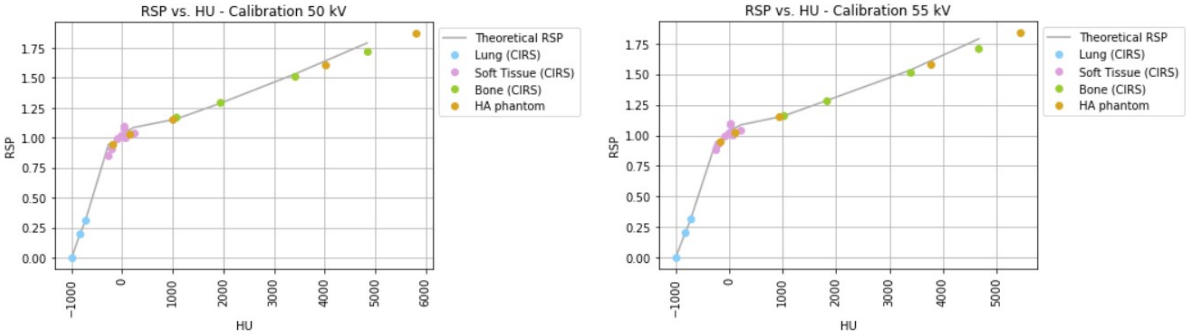

(a) (b)

Figure C.6: In this figure the same stopping powers values of the 18 materials are displayed, now plotted against the CT number. Again, (a) 50 kV and (b) 55 kV.

The same stopping power values can also be plotted against the CT number, as done in figure C.6. It can be seen that the data points follow the line of the calibration curve.

C.3.4. Validation with the HA Phantom

In figure C.7 the middle slices of the CT images of the micro-CT HA phantom are pictured. The different inserts with different concentrations of calcium hydroxyapatite are clearly imaged. Between the two inserts with the highest HA concentrations, an artefact can be observed. This is present in the CT images of both the higher energy and the lower energy.

Figure C.8 shows the relative stopping power of the different inserts from the HA phantom together with the relative stopping power of the CIRS materials. They are plotted with the theoretical stopping power and sorted by their density. It can be seen that the stopping power calculated via the two different calibrations lies close to their theoretical values. It can also be seen that the relative stopping power of the HA phantom follows the same line as that of the bones from the CIRS inserts. Again, there is no big difference noticeable between the two used energies.

For both setups as well as for the validation with the HA phantom, the root mean square error can be seen in table C.3. The average root mean square of the CIRS inserts is 0.03746 and the average root mean square of the validation with the HA phantom is 0.08392.

(a) (b)

Figure C.7: CT images of the micro-CT HA phantom, on the left, scanned with 50 kV, on the right with 55 kV.

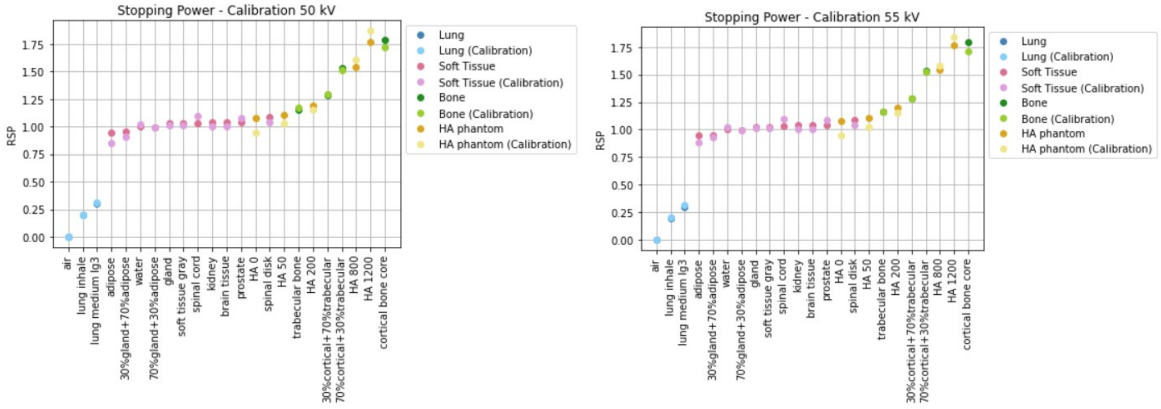

(a) (b)

Figure C.8: In this figure the relative stopping power of the different inserts from the HA phantom are plotted together with the relative stopping power of the CIRS materials, sorted by density. The darker-coloured dots are the theoretical stopping power values and the lighter-coloured dots are the ones calculated via the calibration

	RMSE
Calibration 50 kV	0.0391960
Calibration 55 kV	0.0357300
HA phantom calibration 50 kV	0.0878934
HA phantom calibration 55 kV	0.0799546

Table C.3: This table shows the root mean square error for both setups as well as for the validation with the HA phantom.

C.4. Discussion

C.4.1. CT Imaging

As shown in table C.2, the image quality is higher when using a Median 3D and Gaussian 3D filter after the reconstruction. Because it reduces the amount of noise while still preserving the details, the image quality increases while still giving the same HU values also for smaller objects, which is important in small-animal imaging.

Due to the larger size of the CIRS inserts, a lower energy, as used for small animals such as mice, has more difficulty penetrating through the whole material. To correct for the larger size, 55 kV was used for the first setup. However, this energy will result in a quite high dose for the mice, which are normally scanned with energies around 45-50 kV. To have a better representation of what will be used in preclinical studies, 50 kV was used for the second setup. For the CT calibration, it would be beneficial to have a phantom with the same variety of tissues as the CIRS phantom, however, made based on mice tissue and size instead of human tissue and size. This would enable the use of a lower kV while having the same image quality but also have a more accurate calibration because of the closer representation in terms of tissue composition.

C.4.2. CT Calibration and Stopping Power Calculations

Figures C.3 and C.4 show little difference between the two different setups. This is not that weird, as the two setups are quite similar, only slightly differing in energy. The plots also show the characteristic look of a calibration curve for tissues, with the steepest slope for lung-like tissues, the soft tissues closely together in the same region, and the gentle slope of the bone-like tissue.

When comparing the theoretical stopping power ratios to the SPRs calculated from the calibrations, figures C.5 and C.6 show that both calibrations worked quite well, with not a lot of deviations from the theoretical values can be seen in both setups. The materials that stand out the most regarding their deviation from the theoretical SPR are adipose, spinal cord, and cortical bone core. The SPR of adipose is underestimated by quite a bit, probably due to the fact that the calibration assigns the HU value obtained for adipose to the region with the lung-like tissues. This caused an underestimation of the density and a different elemental composition, both leading to an underestimation of the stopping power ratio of adipose. The calculated SPR value for the spinal cord is an overestimation, with no apparent reason. It could be because of the same reason that adipose is underestimated; the placement of the material in a different region than it should, or it could be due to a differing composition of the insert than the data that we have. Lastly, the SPR of cortical bone is largely underestimated. This seems to be because of its very high density and is also seen in clinical settings.

In general, the calculated SPRs compared to the theoretical SPRs show that both calibrations work well for these inserts and that one is not necessarily better than the other setup.

C.4.3. Validation with the HA Phantom

In figure C.8 the stopping power ratios of the HA phantom are plotted together with the CIRS inserts of approximately the same densities. It can be seen that the different inserts of the HA phantom correspond quite well with the bone inserts from the CIRS phantom. This suggests that the calibration derived from the CIRS inserts can indeed be used for other phantoms or tissues. It can also be seen that for the lower density inserts, there is a decreasing underestimation of the SPR, and for the higher density inserts an increasing overestimation. This seems to be the case for both setups, with no clear difference between the two.

The method used to relate the CT number to the tissue parameters is based on known values determined from human tissues. In order to have a more accurate calibration that can be used in preclinical studies where mouse models are being used, it would be better to base this calibration on data from tissue from mice for a larger accuracy. However, this data is currently not available. Using the HA phantom is already a step in the right direction, however, this phantom only has bone-like tissue, which is not sufficient to base a whole calibration on. Above that, the different regions from the calibration curve that are based on 72 known tissues are also derived from humans. To better divide the different

Insert	Mean HU	SD	Forced HU	SD	SNR	CNR
Air	-1004,785	7,056	-1000	6,726	148,6691	0
Lung inhale	-829,056	12,410	-832,481	11,830	70,36906	14,16027
Lung medium LG3	-726,476	12,663	-734,693	12,071	60,86235	21,97813
Adipose	-239,965	23,732	-270,912	22,623	11,97493	32,22737
30%gland+70%adipose	-188,298	24,093	-221,659	22,967	9,651019	33,88897
Water	44,224	16,621	0	15,844	0	63,11347
70%gland+30%adipose	-60,991	24,524	-100,299	23,378	4,290287	38,4845
100%gland	32,894	27,702	-10,801	26,408	0,408996	37,45863
Soft tissue gray	19,127	27,698	-23,924	26,404	0,906094	36,967
Spinal cord	77,661	27,271	31,875	25,997	1,226101	39,6922
Kidney	104,116	29,700	57,094	28,312	2,016566	37,33673
Brain tissue	100,197	28,163	53,358	26,847	1,987466	39,23524
Prostate	68,414	30,140	23,060	28,732	0,802588	35,60713
Spinal disk	281,559	30,098	226,247	28,692	7,885408	42,73852
Trabecular bone	1169,543	55,160	1072,745	52,583	20,401	39,41856
30%cortical+70%trabecular	2068,378	74,878	1929,587	71,380	27,03269	41,04227
70%cortical+30%trabecular	3633,848	130,275	3421,919	124,189	27,5542	35,60647
Cortical bone core	5118,961	91,805	4837,649	87,516	55,27735	66,70384

Figure C.9: Data CIRS inserts from the CT images acquired with a tube voltage of 50 kV.

mouse tissues into their corresponding regions, a data set from mice tissues should also be used there.

The average root mean square of the CIRS inserts is 0.03746 and the average root mean square of the validation with the HA phantom is 0.08392. It must be taken into account that the calibration is made with the CIRS inserts and the validation is only done with the micro-CT HA phantom, which is located in the range of the bone tissues. Due to the high densities of the bone tissues, the errors are higher than in the range of the soft- and lung-like tissues.

C.4.4. Future Work

Possible next steps, apart from creating a data set based on mouse tissues, as discussed in the previous section, can help improve preclinical proton therapy studies. Firstly, the only validation done in this project was with the HA phantom, so only with bone-like structures. A dosimetric validation with a 3D mouse model would be a useful next step to validate the calibration also in practice. Another interesting step would be to look at dual-energy micro-CT. This can simply be done by scanning two times right behind each other and combining the data of the two scans. This could improve the image quality, which could improve the calibration even further.

C.5. Conclusion

In conclusion, we found that some filtering is needed after the reconstruction to enhance the image quality and also the proton stopping power calibration. Moreover, we found that the calibration as described by Schneider et al. [77], is robust enough to work well for both setups, which is validated with the micro-CT HA phantom. An average RMS of 0.03746 is found for the CIRS inserts, and of 0.08392 for the HA phantom.

C.6. Supplementary Data

All acquired data can be seen below in figure C.9, C.10, C.11, and C.12.

Insert	Mean HU	SD	Forced HU	SD	SNR	CNR
Air	-1014,79	6,045	-1000	5,631	177,5904	0
Lung inhale	-826,836	11,479	-824,920	10,693	77,14784	16,37373
Lung medium LG3	-725,121	11,781	-730,172	10,974	66,53637	24,58781
Adipose	-208,772	18,429	-249,192	17,167	14,51603	43,73639
30%gland+70%adipose	-163,823	19,538	-207,322	18,200	11,39149	43,55446
Water	58,744	15,072	0	14,040	0	71,22704
70%gland+30%adipose	-39,012	21,786	-91,060	20,294	4,487102	44,78922
100%gland	52,261	23,798	-6,039	22,168	0,272418	44,83784
Soft tissue gray	39,623	24,523	-17,811	22,843	0,779717	42,9969
Spinal cord	91,643	24,48	30,646	22,803	1,343913	45,19743
Kidney	120,623	23,891	57,640	22,255	2,590055	47,52472
Brain tissue	116,029	24,142	53,361	22,488	2,372836	46,84032
Prostate	87,690	24,187	26,963	22,530	1,196759	45,58151
Spinal disk	289,263	27,253	214,729	25,386	8,458482	47,84989
Trabecular bone	1142,478	52,907	1009,501	49,283	20,48375	40,77472
30%cortical+70%trabecular	2025,938	75,61	1832,447	70,431	26,01764	40,21595
70%cortical+30%trabecular	3692,760	119,249	3385,096	111,081	30,47418	39,47664
Cortical bone core	5073,296	87,339	4671,070	81,357	57,41481	69,70639

Figure C.10: Data CIRS inserts from the CT images acquired with a tube voltage of 55 kV.

HA concentration	Mean HU	SD	Forced HU	SD	SNR	CNR
0	-146,792	20,111	-182	19,171	9,498086	0
50	158,170	20,505	150,780	19,547	7,713728	17,02931
200	1082,422	30,878	989,694	29,435	33,62258	39,80873
800	4263,100	82,794	4021,773	78,926	50,9563	53,26342
1200	6137,098	110,277	5808,219	105,125	55,25063	56,98278

Figure C.11: Data HA phantom from the CT images acquired with a tube voltage of 50 kV.

Insert	Mean HU	SD	Forced HU	SD	SNR	CNR
Air	-1014,79	6,045	-1000	5,631	177,5904	0
Lung inhale	-826,836	11,479	-824,920	10,693	77,14784	16,37373
Lung medium LG3	-725,121	11,781	-730,172	10,974	66,53637	24,58781
Adipose	-208,772	18,429	-249,192	17,167	14,51603	43,73639
30%gland+70%adipose	-163,823	19,538	-207,322	18,200	11,39149	43,55446
Water	58,744	15,072	0	14,040	0	71,22704
70%gland+30%adipose	-39,012	21,786	-91,060	20,294	4,487102	44,78922
100%gland	52,261	23,798	-6,039	22,168	0,272418	44,83784
Soft tissue gray	39,623	24,523	-17,811	22,843	0,779717	42,9969
Spinal cord	91,643	24,48	30,646	22,803	1,343913	45,19743
Kidney	120,623	23,891	57,640	22,255	2,590055	47,52472
Brain tissue	116,029	24,142	53,361	22,488	2,372836	46,84032
Prostate	87,690	24,187	26,963	22,530	1,196759	45,58151
Spinal disk	289,263	27,253	214,729	25,386	8,458482	47,84989
Trabecular bone	1142,478	52,907	1009,501	49,283	20,48375	40,77472
30%cortical+70%trabecular	2025,938	75,61	1832,447	70,431	26,01764	40,21595
70%cortical+30%trabecular	3692,760	119,249	3385,096	111,081	30,47418	39,47664
Cortical bone core	5073,296	87,339	4671,070	81,357	57,41481	69,70639

Figure C.12: Data HA phantom from the CT images acquired with a tube voltage of 55 kV.

D

Flowchart of Code

This flowchart is an outline of the code that is used. For more details on some steps, see Appendix C.